6-24-2013

Selective Nanoparticles for Antimicrobial Therapies and MRI Diagnostics

Mark Andrew Hoppens
Louisiana State University and Agricultural and Mechanical College

2013

Selective nanoparticles for antimicrobial therapies and MRI diagnostics

Mark Andrew Hoppens
Louisiana State University and Agricultural and Mechanical College, markhoppens@gmail.com

SELECTIVE NANOPARTICLES FOR ANTIMICROBIAL THERAPIES AND MRI DIAGNOSTICS

A Thesis

Submitted to the Graduate Faculty of the
Louisiana State University and
Agricultural and Mechanical College
in partial fulfillment of the
requirements for the degree of
Masters of Science in Biological and Agricultural engineering

in

The Department of Biological and Agricultural Engineering

by
Mark A. Hoppens
B.S., Louisiana State University, 2011
August 2013

I would like to dedicate this dissertation to the outstanding faculty and staff of the Department of Biological and Agricultural Engineering for generously devoting countless time, energy, and concern on my behalf.

ACKNOWLEDGEMENTS

I would like to graciously acknowledge the following people: Dr. Dan Hayes, Dr. Sathivel Subramaniam, and Dr. Marlene Janes for serving on my committee and their council throughout my research, Dr. Todd Monroe, Ammar Qureshi, Alyson Moll, Zanaan Wheeler, Nick Totaro, Cong Chen, Abitha Murugeshu, Christopher Sylvester, Katie Hogan, Jiemin Cormier, Evelyn Gutierrez, and all other lab members for their daily help in countless tasks and hurdles, Dr. Vinod Dasa for sharing his clinical expertise, Dr. Raphael Cueto for his assistance with DLS and zeta potential, Dr. Robert Gambrell for his expertise and help with ICP-OES, Dr. Matt Brown and Ying Xiao for their support in confocal and TEM imaging, Gregory Morrison for his assistance in X-ray diffraction, Dr. George Stanley for his help with FT-IR, Ms. Connie David for her support in HPLC, Tom Scherr for his assistance in image analysis, Randell Deen for his aid in MRI, Dr. David Young for his work with DC magnetic susceptibility, Timothy Machen for his aid in the hemolysis study, and Marilyn Dietrich for her support in flow cytometry. Financial support for this study was provided by the National Science Foundation (Proposal numbers CMMI-963482 and CBET-1254281) and from LSU AgCenter.

TABLE OF CONTENTS

LIST OF ABBREVIATIONS

NP	Nanoparticle
SNP	Silver Nanoparticle (aka SmartSilver^{TM} AS)
CSA	Cationic Steroidal Antimicrobial
MNP	Magnetic Nanoparticle
PAA	Polyacrylic Acid
HPC	Hyroxypropyl Cellulose
TEM	Transmission Electron Microscopy
DLS	Dynamic Light Scattering
MRI	Magnetic Resonance Imaging
DDS	Drug Delivery System
EPR	Enhanced Permeability and Retention
MPS	Mononuclear Phagocyte System
ICP-OES	Inductively Coupled Plasma Optical Emission Spectrometry
DTT	DL-Dithiothreitol
ACN	acetonitrile
HPLC	High Precision Liquid Chromatography
ESI-TOF-MS	Electrospray Ionization -Time of Flight-Mass Spectrometer
FBS	Fetal Bovine Serum

ABSTRACT

Early diagnosis and treatment of an infection and the selectivity of the treatment method are three parameters, which if optimized will greatly enhance a patient's prognosis. Thus these three components have been, and continue to be extensively studied. Advances in biosynthesis and nanofabriciation have provided researchers with new tools with which to improve diagnostic and therapeutic techniques. Of these, inorganic nanoparticles (NPs) have shown great promise. Metallic nanoparticles have been demonstrated to successfully serve as antimicrobials, platforms for the transportation of therapeutic molecules, CT and MRI contrast agents, and thermal ablation. The recent paradigm of theranostics proposes substances that serve both diagnostic as well as therapeutic functions. Metallic nanoparticles are well suited as substrates for multifunctional particles for several reasons including; offering high-density surface ligand conjugation, a reduction in payload degradation, a method of target transfection, and the possibility of controlled release. Additionally, metallic nanoparticles have the benefits of tunable morphologies, large surface area-to-volume ratios, physiologically robust chemistries, and ease of bulk synthesis. Furthermore, functional ligands bound to the NP surface and provide additional functionality such as enhanced solubility, selectivity, and antimicrobial efficacy. This report includes two studies which explore the synthesis and functionality of a theranostic conjugate nanoparticle. Studies were conducted to assess the development of a diagnostic antimicrobial nanoparticle (DAN) comprised of an iron oxide MRI contrast core, an antimicrobial colloidal silver shell, and a selective antimicrobial ceragenin surfactant (CSA-124). The composition of

each component of the DAN has been characterized and its functionality evaluated. Preliminary data has suggested that such a theranostic nanoparticle can successfully be synthesized and its ability as an MRI contrast agent and antimicrobial shows great promise.

CHAPTER 1. INTRODUCTION

As synthetic control, manipulation, and understanding of inorganic nanoparticles and their uses increase, so too does the interest, research, and development in the field. Inorganic nanoparticles are being synthesized and studied for uses as antimicrobials, MRI contrast agents, CT contrast agents, thermal ablation, and delivery platforms for RNA, DNA, peptides, fluorescent markers, and other small molecules[1-7]. The highly specific tunability of inorganic nanoparticles with respect to size, shape, texture, shell thickness, resonance frequencies, and surface chemistries as well as their economic cost and ease of bulk synthesis make them ideal for this wide range of utility [8-10]. Recently several combination nanoparticles have been developed to accomplish multiple functions such as theranostics which both aid in the diagnosis and treatment of disease [11-14]. The following sections address the many specific characteristics of functionalized nanoparticles which impact this project.

1.1 The Clinical Need

The application of this research is primarily to address the clinical problem of deep tissue infections associated with implantation of orthopeadic devices, specifically total knee replacements. Such incidents occur in up to 1.9% of total knee anthroplasties, a surgery that was performed an estimated 800,000 times in 2006 with increasing frequency [15]. Unresolved infections associated with orthopedic implantation can result in implant loosening, anthrodeses, amputations, and possible death [16]. In treating implant related infections, current antibiotic regiments alone have shown to be

insufficient. Often, surgical debridement is necessary which entails resection anthroplasty, systemic antimicrobial treatment, then a re-implantation of the surgical divice. This surgery is terribly invasive and involves an extensive recovery period. Dr. Vinod Dasa of LSU Department of Orthopedic Surgery, a collaborator of this project, states that a major problem associated with implantation related infections is that the exact location of infection often cannot be determined before surgery. The leading culprit of implantation related infection, representing over 50% of incidents, is *Staphylococcus aureus* and coagulase-negative staphylococcus species [15]. For this reason *S. aureus* is the primary test model in this study. Currently employed techniques to combat implantation related infections include using antimicrobial laced bone cements, "clean air measures", and administration of systemic antibiotics at the time of implantation [17]. The objective of this research project has been to develop a selective antimicrobial agent capable of not only combating infection but also indicating the specific location of infection; hopefully preventing the need for such invasive operations.

1.2 Metallic Nanoparticle Background

The most basic characteristic of the metallic nanoparticle is nanoparticle (NP) size. Much research has been conducted regarding NP size with regard to synthesis techniques, vascular retention times, interstitial access, ability to cross the blood-brain barrier, optical properties, and cytotoxicity. It has been demonstrated that particles greater than 200nm in diameter are more prone to activate the complement system and thus be cleared from the circulatory system. Nanoparticles with a diameter under 100nm are capable of penetrating blood vessel pores and NPs under 20nm can access interstitial

spaces [18]. This characteristic has been termed the enhanced permeability and retention (EPR) effect [3, 19]. Another parameter dependent on size is the NP surface area to volume ratio. As the diameter decreases, the relative surface area increases, thus smaller particles are capable of binding and delivering a greater payload per mass NP. That being said, smaller NPs are not always advantageous. Toxicity is also thought to be related to NP size with particles under 100nm having been shown to elicit pulmonary inflammation and oxidative stress [18].

The antimicrobial characteristics of the metallic NP are also of great significance to this study. A vast amount of research has been and continues to be devoted to gold nanoparticles as vehicles of drug delivery and diagnostics, partly due to its bioinert character. Dr. Deepthy Menon and colleagues demonstrated biocompatibility of gold/iron-oxide nanoparticles for concentrations as high as 500 μg/mL and 48 hours incubation with no apoptotic signaling or ROS generation [20]. Silver however is not bioinert and has been shown to be an affective antimicrobial. Silver impacts microbial systems through several mechanisms resulting in the disruption of many crucial cell functions such as cell wall and nucleic acid synthesis, translation, protein structure, and membrane ion pumps. As a result of silver's multiple mechanisms, it is very difficult for a microbe to develop resistance [10, 21]. Silver was also demonstrated to neither elicit genotoxic nor cytotoxic reactions when used as a device coating [22]. Another study showed the EC_{50tox} of SNPs to be between 1000 ppm and 1500ppm [23]. Because of its biocompatibility and antimicrobial nature, silver is currently being incorporated into many products such as medical device coatings, wound dressings, dental resins, and washing machines [2, 10, 21, 23].

Magnetic nanoparticles are also of great interest for their potential as *in vivo* diagnostic agents. Unique optical properties allow some metallic NPs to be used as CT contrast agents [18, 20, 24]. Others possess specific magnetic characteristics highly suited for MRI T1 and T2 contrasting [1, 13, 14, 25-27]. Tagging metallic NPs with fluorescent antibodies is yet another diagnostic technique. The studies herein focus on using ironoxide nanoparticles as a T2 MRI contrast agent. Several iron oxide nanostructures have proven to be highly effective in MRI diagnostics by enhancing negative contrast, some of which are routinely used in clinical applications [27, 28]. Superparamagnetic iron oxide nanoparticles (SPIONs) are one such nanoparticle that has been used clinically with great success as a T2 MRI contrast agent in products such as Feridex, Resovist, and Combidex, which have been used in the diagnosis of spleen, liver, and bone marrow related ailments [27]. Iron oxide contrast agents decrease the T2 relaxation times of water protons in neighboring tissue resulting in dramatically decreasing T2-weighted MRIs signal intensities [1, 12, 29]. They can vary in size from 30-150 nm, and are typically coated in hydrophilic surfactants such as dextran, starch, albumin, silicones, and polyethylene glycol [25]. Required properties for all iron oxide contrast agents include that they must be reasonably magnetic, reach a magnetization greater than 45 emu^{-1}, and be paramagnetic, meaning they only possess a magnetic moment when in the presence of a magnetic field [27].

1.3 Ligand Background

The ligands comprising the surface of conjugate nanoparticles are of extreme importance in that they impact solubility, selectivity, vascular retention times, agglomeration, toxicity, and antimicrobial efficacy.

Surface charge is critical to many of these characteristics. Particles with a moderately neutral charge will be more likely to agglomerate resulting in shorter shelf lives, a lower solubility threshold, and an increased probability of removal from in vivo circulation[1, 30, 31]. Furthermore, cationic ligands have been liked to greater toxicity. Hong et al. and Mecke et al. demonstrated that positively charged dendrimers porate lipid bilayers whereas exposure to neutrally charged dendrimers did not result in pore formation. Leroueil et al. also demonstrated cationic nanomaterials disrupt solid-supported lipid bilayers, irrespective of shape, size, or chemical composition [30]. Once in the body, nanoparticles are removed from circulation; predominantly in the liver and spleen through opsonization, recognition, and removal by the mononuclear phagocyte system (MPS) [32]. In general, neutral to negatively charged nanoparticles with hydrophilic polymer surfaces exhibit prolonged circulation times [31]. It was also demonstrated by Dr. Danscher et.al. that gold nanoparticles were not able to pass the blood-brain or placental barriers but may encounter some simple filtration in the renal glomeruli[33]. Another study suggests that inhaled SNPs are engulfed by alveolar macrophages and experience no significant translocation from the lung to any other organs after seven days[34].

Hydroxypropyl cellulose and polyacrylic acid are two ligands incorporated in the conjugate nanoparticles described in this report. Both polymers have been commonly used to aid in nanomaterial dispersion[35, 36]. They are hydrophilic, negatively charged, nontoxic, and inexpensive. HPC has been widely used in the food industry and PAA can be found in hand sanitizers, toothpastes, and shampoos[37, 38]. Also, PAA is found clinically, used synthetic tear solutions. One study has demonstrated that pharmaceuticals conjugated with HPC exhibit unexpectedly reduced in vivo irritation and concluded HPC to be a suitable pharmaceutical carrier [39]. Another study used HPC as a stabilizer with Naproxen nanosuspentions to achieve greater drug solubility [40]. The LD50 of HPC and PAA for mice is >5g/kg and 4.6 g/kg respectively [41, 42]. It should also be noted at this time, that the PAA used in the nanoparticle conjugates presented in this project is not intended to freely interact with its environment as it is serves as the substrate for the formation of silver shell and attachment of additional ligands.

Another ligand molecule imperative to this study is CSA-124, a synthetic mimic of natural antimicrobial peptides. Antimicrobial peptides are a promising antimicrobial tool as they provide both strain selectivity and novel modes of action capable of circumventing traditional resistance mechanisms. Major problems with these peptides however, are their high cost of bulk synthesis and poor structural stability in the presence of protease. New analogues of antimicrobial peptides, Cationic Steroid Antibiotics (CSA), have been developed which replicate the selectivity and antimicrobial characteristics and offer increased stability and ease of synthesis. CSAs have been shown to be effective against tobramycin-resistant *Pseudomonas aeruginosa*, drug resistant strains of *Helicobacter pylori*, vancomycin-resistant *S. aureus (VRSA)*, and

periodontopathic bacteria such as *Streptococcus mutans* and *Porphyromonas* species [43-45]. Recently Dr. Paul Savage of Brigham Young University synthesized a novel CSA, CSA-124, with a thiol terminated side chain which may allow for specific binding to a nanoparticle surface.

1.4 References

1. Mahmoudi, M., et al., *Toxicity Evaluations of Superparamagnetic Iron Oxide Nanoparticles: Cell "Vision" versus Physicochemical Properties of Nanoparticles.* Acs Nano, 2011. 5(9): p. 7263-7276.

2. Kim, J.S., et al., *Antimicrobial effects of silver nanoparticles.* Nanomedicine-Nanotechnology Biology and Medicine, 2007. 3(1): p. 95-101.

3. Agasti, S.S., et al., *Photoregulated Release of Caged Anticancer Drugs from Gold Nanoparticles.* Journal of the American Chemical Society, 2009. 131(16): p. 5728-+.

4. Nakanishi, J., et al., *Light-Regulated Activation of Cellular Signaling by Gold Nanoparticles That Capture and Release Amines.* Journal of the American Chemical Society, 2009. 131(11): p. 3822-+.

5. O'Neal, D.P., et al., *Photo-thermal tumor ablation in mice using near infrared-absorbing nanoparticles.* Cancer Letters, 2004. 209(2): p. 171-176.

6. Cheng, K., et al., *Magnetic Targeting Enhances Engraftment and Functional Benefit of Iron-Labeled Cardiosphere-Derived Cells in Myocardial Infarction.* Circulation Research, 2010. 106(10): p. 1570-U54.

7. Chertok, B., et al., *Iron oxide nanoparticles as a drug delivery vehicle for MRI monitored magnetic targeting of brain tumors.* Biomaterials, 2008. 29(4): p. 487-496.

8. Yong, K.T., et al., *Synthesis and plasmonic properties of silver and gold nanoshells on polystyrene cores of different size and of gold-silver core-shell nanostructures.* Colloids and Surfaces a-Physicochemical and Engineering Aspects, 2006. 290(1-3): p. 89-105.

9. Jackson, J.B. and N.J. Halas, *Silver nanoshells: Variations in morphologies and optical properties.* Journal of Physical Chemistry B, 2001. 105(14): p. 2743-2746.

10. Pal, S., Y.K. Tak, and J.M. Song, *Does the antibacterial activity of silver nanoparticles depend on the shape of the nanoparticle? A study of the gram-*

negative bacterium Escherichia coli. Applied and Environmental Microbiology, 2007. 73(6): p. 1712-1720.

11. Chen, X., Gambhir, Sanjiv, *Theranostic Nanomedicine Editorial.* Accounts of Chemical Research 2011. 44(10): p. 841-1134.

12. Narayanan, S.e.a., *Biocompatible Magnetite/Gold Nanohybrid Contrast Agents via Green Chemistry for MRI and CT Bioimaging.* Applied Material Interfaces, 2011. ASAP.

13. Jose L. Del Pozo, R.T., *Infection Associated with Prosthetic Joints.* The New England Jounral of Medicine, 2009(361): p. 787-794.

14. Hickok, N.J. and I.M. Shapiro, *Immobilized antibiotics to prevent orthopedic implant infections.* Advanced Drug Delivery Reviews, 2012.

15. Chiu, F.Y., et al., *Cefuroxime-Impregnated Cement in Primary Total Knee Arthroplasty A Prospective, Randomized Study of Three Hundred and Forty Knees.* The Journal of Bone & Joint Surgery, 2002. 84(5): p. 759-762.

16. Emerich, D.F. and C.G. Thanos, *The pinpoint promise of nanoparticle-based drug delivery and molecular diagnosis.* Biomolecular Engineering, 2006. 23(4): p. 171-184.

17. Chertok, B., et al., *Iron oxide nanoparticles as a drug delivery vehicle for MRI monitored magnetic targeting of brain tumors.* Biomaterials, 2008. 29(4): p. 487-496.

18. Qureshi, A.T., et al., *Biocompatible/bioabsorbable silver nanocomposite coatings.* Journal of Applied Polymer Science, 2011. 120(5): p. 3042-3053.

19. Jung, W.K., et al., *Antibacterial activity and mechanism of action of the silver ion in Staphylococcus aureus and Escherichia coli.* Applied and Environmental Microbiology, 2008. 74(7): p. 2171-2178.

20. Na, H.B., I.C. Song, and T. Hyeon, *Inorganic Nanoparticles for MRI Contrast Agents.* Advanced Materials, 2009. 21(21): p. 2133-2148.

21. Schweiger, C., et al., *MRI contrast enhancement potential of different superparamagnetic iron oxide nanoparticle (SPION) formulations.* Journal of Controlled Release, 2010. 148(1): p. E67-E68.

22. Babes, L., et al., *Synthesis of iron oxide nanoparticles used as MRI contrast agents: A parametric study.* Journal of Colloid and Interface Science, 1999. 212(2): p. 474-482.

23. Moghadam, B.Y., et al., *The Role of Nanoparticle Surface Functionality in the Disruption of Model Cell Membranes.* Langmuir, 2012.

24. Perry, J., et al., *PEGylated PRINT Nanoparticles: The Impact of PEG Density on Protein Binding, Macrophage Association, Biodistribution, and Pharmacokinetics.* Nano Letters, 2012.

25. Bilbao-Sáinz, C., et al., *Composite edible films based on hydroxypropyl methylcellulose reinforced with microcrystalline cellulose nanoparticles.* Journal of agricultural and food chemistry, 2010. 58(6): p. 3753-3760.

26. Mergel, M., *Polyacrylic Acid*, S.G. Gilbert, Editor. 2010, Toxipedia.

27. Nancy M. Franson, D.R.S., *Milled naproxen with hydroxypropyl cellulose as a dispersion stabilizer*, USPTO, Editor. 1997, NanoSystems L.L.C., Collegeville, PA: USA.

28. Ain-Ai, A. and P.K. Gupta, *Effect of arginine hydrochloride and hydroxypropyl cellulose as stabilizers on the physical stability of high drug loading nanosuspensions of a poorly soluble compound.* International journal of pharmaceutics, 2008. 351(1): p. 282-288.

29. Williams, R., *HYDROXYPROPYL CELLULOSE*, in *Material Safety Data Sheet:*. 2001, USP.

30. SIGMA-ALDRICH, *POLY(ACRYLIC ACID)*, in *MATERIAL SAFETY DATA SHEET*. 2006: 3050 Spruce StreetSAINT LOUIS MO 63103 US.

31. Leszczynska, K., et al., *Bactericidal activities of the cationic steroid CSA-13 and the cathelicidin peptide LL-37 against Helicobacter pylori in simulated gastric juice.* Bmc Microbiology, 2009. 9.

32. Bucki, R., et al., *Resistance of the antibacterial agent ceragenin CSA-13 to inactivation by DNA or F-actin and its activity in cystic fibrosis sputum.* Journal of Antimicrobial Chemotherapy, 2007. 60(3): p. 535-545.

33. Leszczynska, K., et al., *Potential of ceragenin CSA-13 and its mixture with pluronic F-127 as treatment of topical bacterial infections.* Journal of Applied Microbiology, 2011. 110(1): p. 229-238.

CHAPTER 2. SYNTHESIS AND CHARACTERIZATION OF CERAGENIN FUNCTIONALIZED IRON CORE, SILVER SHELL NANOMATERIALS

Brief Summary: New synthesis techniques are providing increasing control over many inorganic nanoparticle characteristics, facilitating the creation of new multifunctional theranostics, or therapeutic and diagnostic agents. This report proposes the synthesis of a combination nanoparticle comprised of an iron oxide core for enhanced T2 MRI contrast diagnostics, a colloidal silver shell acting as an antimicrobial and therapeutic vehicle, and a cationic steroid antibiotic (CSA) surfactant providing microbial selectivity. Herein we present new methodology for iron core, silver shell nanoparticle (NP) synthesis and functionalization. A polyacrylic acid functionalized iron nanoparticle is synthesized by a high temperature organic phase reduction followed by thiol functionalization and gold cluster seeding. A silver shell is formed through $AgNO_3$ reduction, and an oriented monolayer of the thiolated ceragenin, CSA-124, is bound through a self-assembly process. The process and products are characterized throughout synthesis through TEM, DLS, FT-IR, UV-Vis, ICP-OES, HPLC-ESI-TOF-MS, DC magnetization and susceptibility, X-ray diffraction, and *in vitro* MRI. Synthesized Diagnostic Antimicrobial Nanoparticles (DANs) were found to have a spherical morphology with a diameter of 32.47 $^{+}$/- 1.83 nm, a hydrodynamic diameter of 53.05 $^{+}$/- 1.20 nm, a maximum magnetic moment of 12 emu/g NP, or 54 emu/g Fe, with little variation due to temperature, and be predominantly paramagnetic. X-ray diffraction advocates that the iron oxide core is maghemite. *In vitro* MRI studies show that DANs contrast well as concentrations as low as 9 ppm, and successfully adhere to and *S. aureus.*

2.1 Introduction

As synthetic control, manipulation, and understanding of inorganic nanoparticles increase, so too does the interest, research, and development in the biomedical field. Inorganic nanoparticles are being synthesized and studied for use as antimicrobials, MRI contrast agents, CT contrast agents, thermal ablation targets, and delivery platforms for RNA, DNA, peptides, fluorescent markers, and other small molecules.[1-7] The highly specific tuneability of inorganic nanoparticles with respect to composition, morphology, shell thickness, resonance frequencies, and surface chemistries as well as their economical and facile bulk synthesis make them ideal for this wide range of applications.[8-10] Recently several hybrid nanoparticles have been developed to accomplish multiple functions, such as in theranostics wherein the particle both aids in the diagnosis and treatment of disease.[11, 12]

Superparamagnetic iron oxide nanoparticles (SPIONs) are one such inorganic nanoparticle that has been used clinically with great success as a T2 contrast agent for magnetic resonance imaging (MRI). SPIONs are the primary active component of products such as Feridex, Resovist, and Combidex, which have been used in the diagnosis of spleen, liver, and bone marrow related ailments.[27] Iron oxide contrast agents work by decreasing the T2 relaxation times of water protons in neighboring tissue and dramatically decreasing signal intensities in T2-weighted MRIs.[1, 12, 29] They can vary in size from 30-150 nm and may be coated in dextran, starch, albumin, silicones, polyethylene glycol, and many other hydrophilic surfactants.[25] One property common to all MRI contrast agents is that they must be paramagnetic, meaning they only possess a

magnetic moment when in the presence of a magnetic field and this induced magnetization should be on the order of 45 emu g^{-1}. [27]

Among inorganic nanoparticles, silver has shown to be an affective antimicrobial as well as therapeutic carrier agent. Silver has been demonstrated to deactivate bacteria through several different mechanisms, thereby making it very difficult for an antimicrobial to develop resistance.[46] Because of its biocompatibility and antimicrobial nature, silver is currently being incorporated into many products such as dental resins, medical device coatings, wound dressings, and washing machines.[2, 10, 21] Furthermore, noble metal nanoparticles such as silver, also offer an attractive vehicle for small molecule delivery due to their robust functionalization chemistries, large surface area/volume ratios, readily tunable morphologies, and ease of bulk synthesis.[47] They also offer high-density surface ligand attachment and reduced degradation of the therapeutic agent.[18, 48, 49]

Antimicrobial peptides, which provide bacterial membrane selectivity and novel modes of action, are a promising means of controlling bacterial growth because they are capable of circumventing traditional resistance mechanisms. However, several constraints to the general clinical use of these peptides are their high cost of bulk synthesis and poor structural stability in the presence of proteases. New mimics of antimicrobial peptides, ceragenins or CSAs, have been developed which mimic the selectivity and antimicrobial characteristics of antimicrobial peptides while offering increased stability and ease of synthesis. CSAs have been shown to be effective against tobramycin-resistant *P. aeruginosa*, drug resistant strains of *H. pylori*, vancomycin-resistant *S. aureus (VRSA)*,

and periodontopathic bacteria such as *Streptococcus mutans* and *Porphyromonas* species.[43-45]

This report describes a synthesis procedure for the creation of Diagnostic Antimicrobial Nanoparticles (DANs) comprised of an iron oxide core, reduced silver shell, and CSA-124 surfactant for the purpose of selectively diagnosing and treating microbial infections. The synthetic process and resulting materials are characterized by several methods including transmission electron microscopy (TEM), dynamic light scattering (DLS), Fourier transform infrared spectroscopy (FT-IR), Inductively coupled plasma optical emission spectrometry (ICP-OES), ultraviolet-visible spectroscopy (UV-Vis), High Performance Liquid Chromatography – Electrospray Ionization tandem Time Of Flight Mass Spectrometry (HPLC-ESI-TOF-MS), and DC magnetization and susceptibility. It is the objective of this study to present a viable synthesis procedure by which to consistently synthesize DANs as well as demonstrate their selective diagnostic potential.

2.2 Material and Methods

Materials:

The following materials were ordered from Sigma-Aldrich®: polyacrylic acid (average MW 1800), triethylene glycol (99%), iron acetylacetonate (99.9%), ethyl-dimethyl-aminopropylcarbodiimide, cysteamine hydrochloride (≥98%), 2-(N-morpholino)ethanesulfonic acid, silver nitrate(>99%), ammonium hydroxide (28-30%), N-hydroxysulfosuccinimide (98.5%), sodium hydroxide (NaOH), tetrakis(hydroxymethyl)phosphonium chloride (THPC, 80% in water), tetrachloroaurate

trihydrate ($HAuCl_4$), and dialysis membranes (10,000 Da). Acetic acid (99%) was obtained from Fisher Scientific®. Formaldehyde (36.5-38%) was obtained from Mallinckrodt Chemicals®. CSA-124 was prepared by functionalizing a ceragenin, CSA-13, with a thiol group on a short PEG tether. Synthetic details for CSA-124 will be reported elsewhere. All other chemicals were used as received unless otherwise noted. Mueller Hinton Broth, and Nutrient Agar, pH6.0 with 0.8%NaCl was purchased from Himedia®/VWR™.

Methods: DAN synthesis

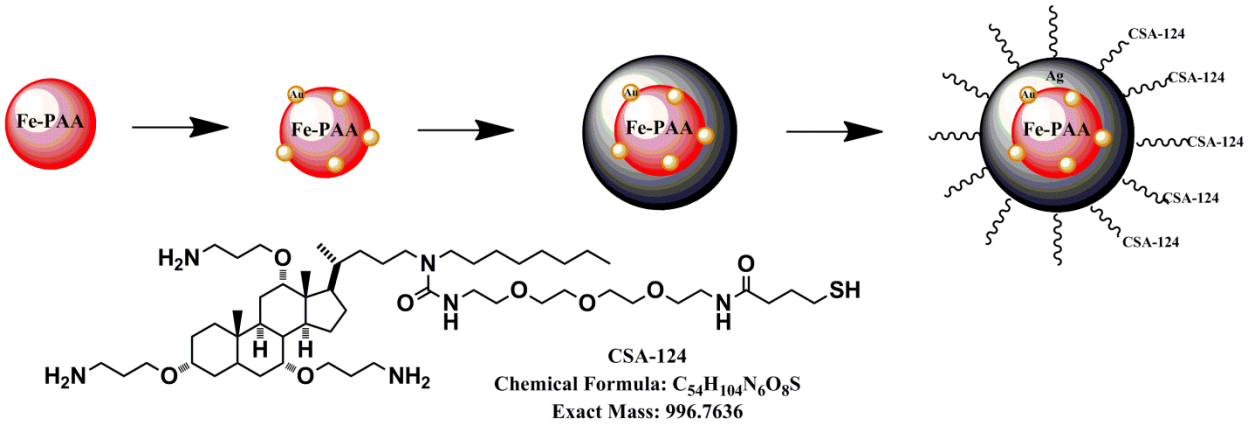

Figure 1.1 An overview of the synthesis process is presented. Fe-PAA NPs are synthesized; they are then functionalized and seeded with gold NPs (1). Silver ions from $AgNO_3$ are reduced onto the gold particles (2). Finally, CSA-124 is bound to the surface of the silver shell (3).

Polyacrylic Acid-Coated Iron Nanoparticle Synthesis

Iron-Polyacrylic Acid nanoparticle (Fe-PAA NP) synthesis was based on the thermal decomposition methods employed by Ming Ling et al.[35] All reactions were

conducted in an argon atmosphere. First, 1.0 gram of polyacrylic acid was added to 25 ml triethylene glycol, followed by the addition of 2.0 mM (706 mg) iron acetylacetonate ($Fe(acac)_3$) solution and stirred until dissolved. Using a Glas-Col 500 mL, 325 watt heating mantle regulated by a Glas-Col power regulator the mixture was slowly heated to 190˚ C over 30 minutes, then rapidly heated to reflux at 275˚ C where the temperature was held for 20, 30, or 40 minutes.

To purify the resulting mixture, 30 mL ethyl acetate (EtOAc) was added. The mixture was then shaken and centrifuged at 5870x*g* for 30 minutes. The supernatant (EtOAc and dissolved impurities) was removed and discarded. The black precipitate was further purified via liquid/liquid extraction by first re-suspending in 5-10 mL DI water and then adding 20-30 mL EtOAc, centrifuging once at 3000 g for 5 minutes, and removing the supernatant of EtOAc and dissolved impurities. The liquid/liquid extraction process was repeated for a total of two iterations. Removal of residual EtOAc was accomplished via dialysis (MW cutoff 10,000 Daltons) over a 24-36 hour period. This procedure yielded a solution of 28.5 ppm iron content. The Fe-PAA NPs were characterized using TEM, DLS, ICP-OES, and FT-IR.

Thiol Functionalization

The functionalization protocol was as follows: for each 1 mL of Fe-PAA NP used, 0.4 mL 2-(N-morpholino)ethanesulfonic acid (MES buffer) at 500 mM and 2.6 mL DI water were added and mixed. Next, 3.5 mL EDC/sulfo-NHS solution (52 mM EDC & 10.13 mM Sulfo-NHS) was added to the solution and allowed to react at 37˚ C and under

gentle agitation for 30 minutes. To this solution, 0.5 mL cysteamine hydrochloride at 0.265mM was added and left to react at room temperature for four hours. Purification was conducted by 24 hour dialysis, during which time the water bath was exchanged three times. This procedure yielded an 8.0 mL solution of 2.75 ppm iron content.

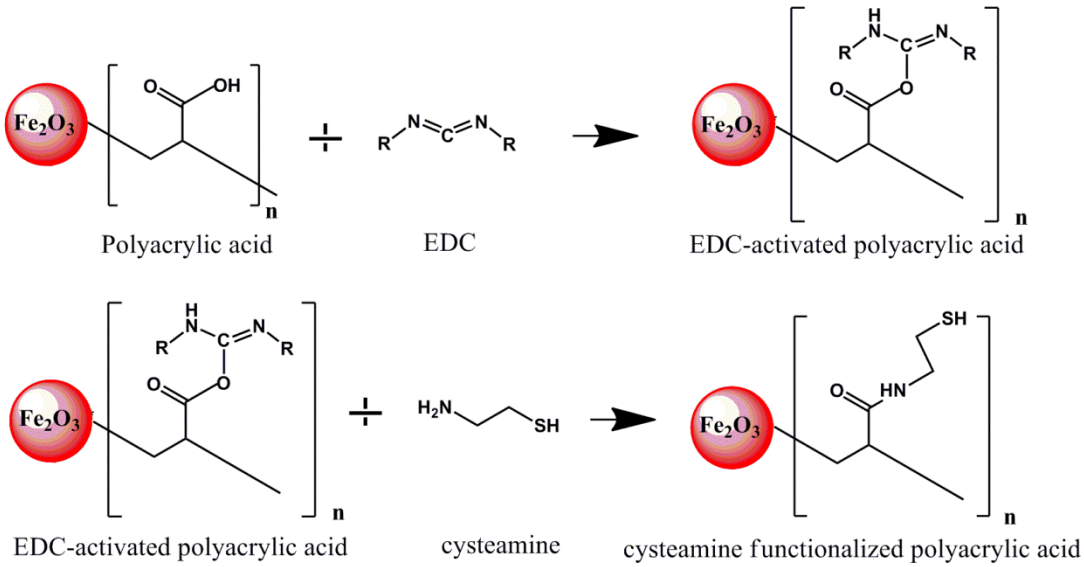

Figure 2.2 Functionalization schematic of the PAA surfactant through an EDC/Sulfo-NHS workup. Carboxylic acids are activated with EDC then functionalized with cysteamine, resulting in terminal thiols allowing for strong gold seed adhesion.

Gold Nanoparticle Synthesis

Gold NPs with approximate diameters of 5 nm were prepared using a modified procedure outlined by Duff *et. al.* Briefly, 1.0 mL of 0.06 mmol NaOH and 2 mL of THPC (12 µL in 1 mL of DI water) were mixed with 200 mL of DI water. After 15 min, 4 mL of 1% (w/v) aqueous $HAuCl_4$ was added and continued to stir for an additional 40 min. The solution immediately transitioned from clear to a red-yellow colored solution. Before use, the gold NPs were refrigerated and aged for 3 days.

Gold Seeding

A 3 mL aliquot of gold NP solution (18.7 ppm) was mixed with the 8 mL thiol-functionalized MNP solution for 3 hours at 25˚ C. The sample was then centrifuged at 9180x*g* for ten minutes. Centrifugation was repeated for a total of three times, removing the supernatant between each iteration. After completion of the third centrifugation, the precipitant was resuspended in 2.5 mL DI water, resulting in a solution of 0.300 ppm iron content. The concentrations of gold seeded iron nanoparticles (Au-Fe-PAA) were measured using ICP-OES and images were obtained using TEM (specific protocols below).

Silver Shell Formation

Silver shell formation was conducted according to a modification of the method of the Jackson *et al.*[9] Silver was reduced on the gold seeded, iron core as follows: 2.0 mL of 5 mM $AgNO_3$ was added to the 2.5 mL Au-Fe-PAA NP solution and mixed. Seventy micro liters of formaldehyde solution (36.5-38%) was then added and mixed. Finally, 20 μL ammonium hydroxide (28-30% NH_3 content) was added in 5 μL increments, stirring between additions. After the addition of ammonium hydroxide, a visible change in color from translucent purple-brown to dark brown-black was observable with the unaided eye. This procedure yielded a 4.6 mL solution of 60.5 ppm iron content.

CSA Self Assembly

Immediately after completion of the silver coating process, 50 μL of 0.17 mM CSA solution (CSA, DI water, and acetic acid at a pH 4.5) was added and mixed for 1 hour. The resulting nanoparticle solution was purified via dialysis as described above.

Methods: Nanoparticle Characterization

Fourier Transform Infrared Spectroscopy (FT-IR):

FT-IR measurements and analysis were performed on freeze-dried samples of Fe-PAA nanoparticles and cysteamine functionalized Fe-PAA NP using a Bruker Tensor 27 FT-IR using a standard room-temperature DTGS detector & OPUS 6.5 Data Collection Program. The freeze-dried samples were ground onto the surface of a KBR plate and measured. The absorbance values were normalized against a KBR plate with no sample.

Ultraviolet-Visible Spectroscopy (UV-Vis):

The UV-Vis results were obtained using a ThermoSpectronic Genesys 6 (Rochester, NY) using Malvern ZEN0040 disposable cuvettes. Nanoparticle samples were diluted to roughly 0.02 ppm in DI water and filtered using a Thermo Scientific Nalgene 0.2μm surfactant-free cellulose acetate membrane. Absorbance was recorded from 200-700nm at 25˚ C.

X-Ray Diffraction

The core-shell nanoparticles were characterized by powder X-ray diffraction to determine the structure of the iron oxide core. Diffraction experiments were performed using a Bruker Kappa APEX II CCD single crystal diffractometer equipped with a Mo K_α source (λ = 0.71073 Å) and graphite monochromator. Approximately 0.1 mg of core-shell nanoparticles was adhered to the tip of a MiTeGen fiber using Paratone-N oil. A series of five phi scans (image width = 180 °) were then collected with different detector orientations covering a 2θ range of 10-50 ° at a detector distance of 100 mm. These images were merged and integrated using the XRD^2 Eval program in the Bruker APEX2 software. A background subtraction was applied using the EVA 2 program.

Dynamic Light Scattering (DLS):

Hydrodynamic diameters were measured using a Malvern Zetasizer nano series (Worcestershire, UK). NP samples from various stages of synthesis were diluted to roughly 0.02 ppm in $NaHCO_3$/DI (100 mM) then filtered using a Thermo Scientific Nalgene 0.2 μm surfactant-free cellulose acetate membrane. Samples were measured in Malvern ZEN0040 disposable cuvettes at 25˚ C.

Transmission Electron Microscopy (TEM):

The TEM images were obtained using a JOEL 2011 TM (Tokyo, Japan). Nanoparticle samples were diluted to roughly 25 ppm in DI water and 5 μL was applied to an Electron Microscopy Sciences carbon film 400 square mesh copper grid and allowed to air dry. Images were taken at 150,000X. TEM images were analyzed using

Metamorph Advanced software. The diameters of 25 nanoparticles of each type were measured using digital calipers and statistical significance was determined using a one sample t-test.

CSA Quantification by High Performance Liquid Chromatography – Electrospray Ionization tandem Time Of Flight Mass Spectrometry (HPLC-ESI-TOF-MS)

A five point standard curve, $R^2 = 0.9942$, was constructed by comparing known concentrations of CSA-124 dissolved in 25% $^{v}/_{v}$ acetonitrile (ACN) in DI to the integrated area of its HPLC-ESI-TOF-MS peak. CSA-124 displaced from DANs and run through HPLC-ESI-MS/MS were then quantified by comparison to this standard curve. To remove CSA from the DAN, 5.5 µL DL-Dithiothreitol (DTT) was added to 500 µL CSA-SNPs and allowed to react for one hour at 37° C. The DTT displaces the CSA from the SNP surface resulting in DTT-SNPs and a solution of CSA and unreacted DTT. This was then separated via centrifugation for 15 minutes at 12xg. The supernatant was removed and concentrated from 500 µL to 250 µL by vacufugation and 250 µL of ACN/DI (50% v/v) was then added to the solution bringing the final solution to 25% ACN. The samples were then analyzed by HPLC-ESI-TOF-MS (Agilent 1200 with a binary pump/Agilent ESI TOF 6210 PALO ALTO, CA). The LC column used was a normal phase Acclaim® Mixed-Mode HILIC-1, 3µm Analytical (2.1 x 150mm). Samples and standards were injected at 2 µL. The first mobile phase was 90% ACN in water with 0.1% formic acid while the second mobile phase was water with 0.1% formic acid. The ESI parameters used are as follows: nitrogen temperature 325° C, nitrogen flow 5 L/min,

nebulizer pressure 20 psi. The DTT-SNP pellet obtained from the previously mentioned centrifugation was quantified by ICP-OES.

Inductively Coupled Plasma Optical Emission Spectrometry (ICP-OES):

ICP-OES data were collected using a Varian Vista MPX (Palo Alto, CA). The mass of a 10mL glass test tube was recorded, 100µL of NP sample, 1mL nitric acid, and 10mL of DI water were added. Masses were recorded after each addition. The iron, silver, and gold concentrations of this solution were measured by the Vista MPX. Using these results and the component densities, the concentrations of the original samples were calculated.

DC magnetization and susceptibility:

The magnetic properties of the nanoparticles were measured with a Quantum Design Physical Property Measurement System (PPMS) using the ACMS option. This utilizes a DC, Faraday-extraction technique in which the sample is quickly pulled (at a speed of 100 cm/s) through a set of detection coils. Zero-field cooled (ZFC) and field-cooled (FC) magnetic susceptibility data were measured as a function of temperature at a constant field of 1000 Oe. The magnetic hysteresis of the nanoparticles was determined from the field dependence of the DC magnetization from 0 to ±9 T at a temperature of 3 K.

Contrast Concentration Dependence

To determine contrast dependence on DAN concentration, five 1.5 mL centrifuge tubes were filled with an agarose/ DAN solution and imaged with MRI at the following concentrations: o ppm, 1.6 ppm, 3.3 ppm, 9.8 ppm, and 27.9 ppm. Also, to determine the impact the DAN's silver shell has on its contrast capabilities, five 1.5 mL centrifuge tubes were filled with a solution of agarose and the iron oxide core at the following concentrations: 0.0 ppm, 1.6 ppm, 3.3 ppm, 9.6 ppm, and 26.6 ppm. These ten samples were aligned and imaged in a single image using the following parameters: TR: 3000, TE: min/full, EC: 1/1 41.7 kHz, FOV: 16x12/z, thickness 6 mm. The resulting image was analyzed using image J and the gray scale values of each sample were recorded.

Magnetic Resonance Imaging

Sample preparation for magnetic resonance imaging (MRI) was conducted as follows. 10 mL of Muller Hinton Broth (MBH) was inoculated with one loop of *S. aureus* and incubated 24 hours at 37˚ C. Three mL of inoculated broth was then added to two test tubes. To one of these test tubes 300 µL DANs at 200 ppm was added, while the other test tube received 300 µL Ag-Au-Fe-MNP (no CSA) at 200 ppm. Two other test tubes were prepared by adding 3 mL DI and 300 µL DANs. These four solutions were allowed to rest at room temperature for 30 minutes, then all were filtered through a 0.45 µm, surfactant-free, cellulose acetate syringe filter with the exception of one of the DAN/DI samples which serves as a positive control and was filtered using a 0.2 µm filter. The filters were removed from their casing and suspended in the center of at block of

agarose approximately 2”x3”x3” in size. All samples were imaged under the following parameters: TR: 3000, TE: min/full, EC: 1/1 41.7 kHz, FOV: 16x12/z, thickness 1mm.

2.3 Results and Discussion

The DANs synthesis is a multi-step procedure and is outlined in Figure 1. The core of the DAN is an iron nanoparticle with a polyacrylic surface ligand (Fe-PAA) synthesized through thermal reduction of iron oxide in an organic solvent. After synthesis, the polyacrylic acid surfactant is modified with cysteamine through an ethyl-dimethyl-aminopropylcarbodiimide (EDC) chemistry reaction (described in Figure 2), resulting in a distal thiol group on the polyacrylic that will readily bind with gold and silver. The cysteamine “activated” product is then reacted with gold nanoparticles, or “seeds”, which interact with functionalized Fe-PAA through thiol linkages.[50] This seeded surface provides nucleation sites for silver reduction and shell formation resulting in a colloidal shell several nanometers thick. Lastly, the CSA-124 is attached to the silver shell via its thiolated ethylene glycol side chain providing a uniform orientation of the compound with two primary amines on the distal portion of the molecule free to interact with the environment.

Functionalization of the iron with polyacrylic acid provides for a hydrophilic particle improving colloidal solubility in the follow-on aqueous reactions. Additionally the PAA surfactant provides a platform for gold seeding and colloidal shell formation. The functionalization procedure of PAA was modified from of the protocol Ken-Tye Yong *et al.* developed for the functionalization of carboxylate modified polystyrene beads[8]. The carboxyl groups of the PAA were activated by ethyl-dimethyl-

aminopropylcarbodiimide (EDC) and N-hydroxysulfosuccinimide (Sulfo-NHS), and then reacted with the primary amine groups of cysteamine hydrochloride (CH), resulting in an amide bond linkage. An EDC/Sulfo-NHS workup is a well-established, facile method for bonding molecules through their carboxylic and amine groups and has also been utilized in CA/BMPA-coating magnetic nanoparticles,[51] protein coupling, [52] and protein film deposition.[53] Once bound to the NP surface, the cysteamine offered a primary thiol group that was ideal for the attachment of colloidal gold used in shell growth.

The method of colloidal attachment of gold nanoparticles to the thiol-functionalized PAA and silver reduction was based on a method previously presented by Jackson and Halas.[9] In our modification, silver from $AgNO_3$ was reduced onto the gold seed nucleation sites bound to the PAA through cysteamine. This method provides adequate control over shell thickness while maintaining colloidal stability in follow-on aqueous CSA functionalization reactions. The CSA functionalization reaction is conducted immediately following silver shell reduction to add bulky surface groups providing steric hindrance and bound surface charges to reduce agglomeration of the finished particles. If surface functionalization is not conducted within hours of the silver reduction step, particles will rapidly agglomerate.

The composition of the nanoparticles was analyzed using FT-IR, ICP-OES, and UV-VIS. FT-IR was employed to verify the addition of cysteamine to the carboxy terminus of the polyacrylic acid surfactant on the Fe-PAA NP. In this reaction, a carboxyl group is converted into an amide bond (as seen in Figure 3). The FT-IR peaks for carboxyl and amide groups are commonly found at 1780-1710 cm-^{1} and 1690-1620 cm^{-1}, respectively.[54] In the FT-IR spectra of Fe-PAA NPs in Figure 3a there is a clear peak at

1726 cm^{-1} indicative of the carboxyl group. In Figure 3b the 1726 cm^{-1} maxima peak is greatly reduced while a clear peak arises with a 1619 cm^{-1} maxima indicating that many, though not all, of the carboxyl groups have been converted to amides.

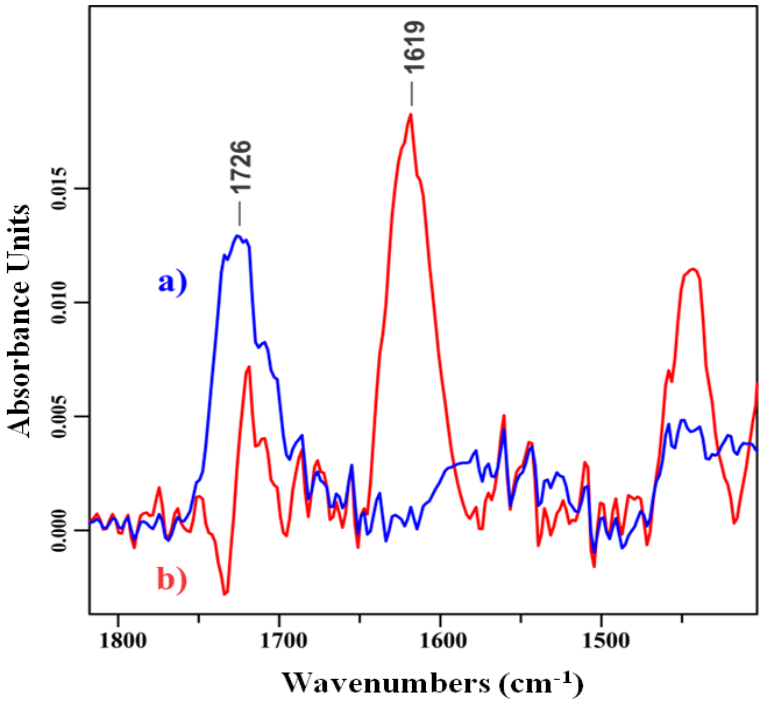

Figure 2.3 The FT-IR spectra shown indicate a shift in bond energy upon functionalization of Fe-PAA with cysteamine.

Through ICP-OES, concentrations of iron, gold, and silver were monitored throughout the synthesis process. Using this information and the known sample volumes it was possible to track the mass balance of each element. ICP-OES data shows that the compositions of DANs are 76.64% silver, 22.75% iron, and 0.61% gold. Based on the mass balance of iron, it was determined that the synthesis procedure from Fe-PAA NPs through functionalization, gold seeding, and silver coating resulted in a 8.6 percent yield with the bulk of losses being attributed to centrifugal purification. It is suspected that substituting magnetic separation for centrifugation during the purification process could minimize these losses. Iron was chosen to be the element monitored for percent yield

because it was the only element added in the first step and not introduced again throughout the process.

UV-VIS spectroscopy was used to monitor to process progress between steps. After NP-PAA functionalization, curve "a" in Figure 4 was obtained. This curve served as a baseline or comparison point for subsequent measurements. Curve "b" represents the UV-Vis spectra obtained after purification of gold seeded Fe-PAA NPs. This curve clearly differs from the baseline curve and closely parallels the absorbance spectra of a gold NP control (Supporting Information section).

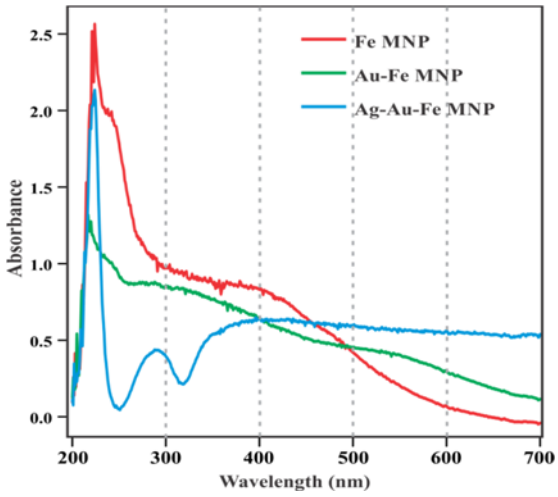

Figure 2.4 UV-Vis absorption spectra of DANs at different stages of development are shown. Series (a) shows Fe-PAA NP, (b) shows Au-Fe-PAA NP, and (c) shows Ag-Fe-PAA.

The similarity between the Au-MNP and gold seed control curves supports the assertion that gold seeds were successfully attached to the PAA coating of the iron NPs. Curve "c" depicts the absorbance spectra obtained after silver was reduced onto the Au-Fe-PAA. As with the gold seeded NPs, the silver coated NP curve is distinctly different from both the previous curves and shows the clear red shifting commonly associated with

metal nanoshell synthesis.[9] This strongly indicates that a silver shell was successfully reduced onto the particle surface, thus supporting the ICP-OES findings.

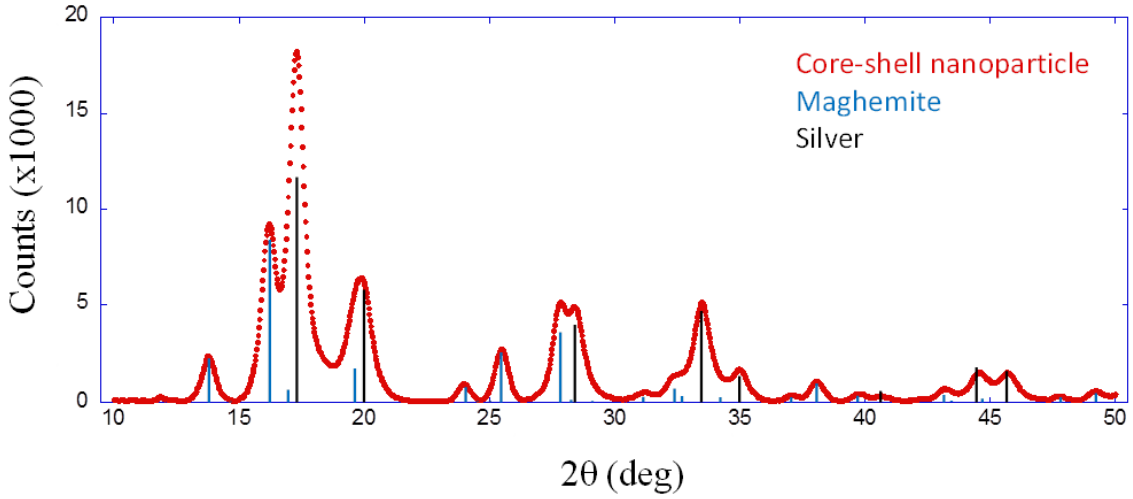

Figure 2.5 X-ray diffraction pattern of DAN core

To determine the exact structure of the DAN's iron oxide core, x-ray diffraction was employed. A powder diffraction pattern of the core-shell nanoparticles is shown in Figure 2.5. The reflections due to the iron oxide core are indexed as blue lines and the reflections due to the silver shell are indexed as black lines. The indexed reflections indicate that the iron oxide core is maghemite. This is consistent with the brown color of the core nanoparticles.

The shape and size of nanoparticles at various stages of synthesis were determined using a combination of TEM and DLS. The TEM images displayed in Figure 6 show the growth of the nanoparticles as gold seeds were attached (Figure 6b) and a silver shell was reduced onto the Fe-PAA NP (Figure 6c). It is also evident that the Fe-

PAA NPs have a rough spherical morphology that became more regular and smooth as gold and silver were added in following processes.

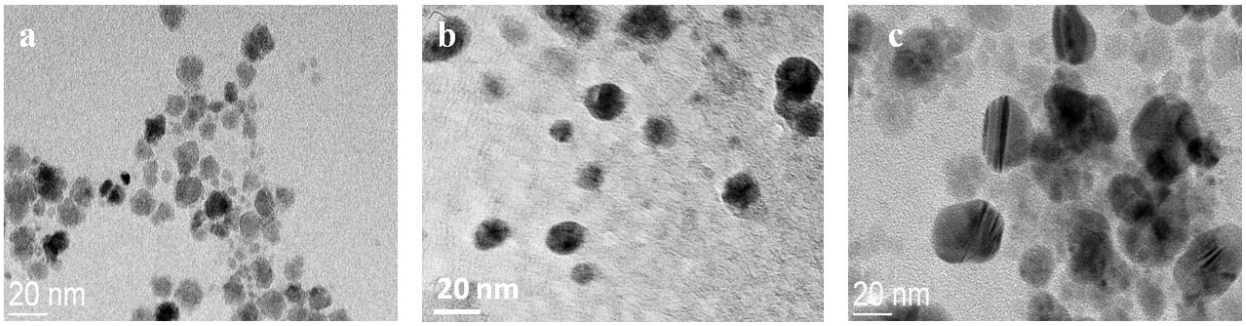

Figure 2.6 TEM images of the nanoparticles at three stages of development are shown: (a) Fe-PAA nanoparticles, (b) Au-Fe-PAA, and (c) Ag-Fe-PAA with CSA-124 surfactant.

Analysis of the TEM images using Advanced Metamorhph was used to determine nanoparticle size and is presented in Table 1. One sample t-test analysis of these values found that the diameter increase after gold seeding was not statistically significant ($P>0.05$) while the diameter increase after silver shell reduction was ($P<0.05$). Hydrodynamic diameters, as determined through DLS, are also included in Table 1. As expected from a reasonably monodisperse product there is substantial agreement between the values generated from the TEM image and the DLS results. As the multi-step synthesis continues larger particles with larger hydrodynamic diameters are produced as a result of the addition of the silver coating and CSA-124 addition.

Table 2.1 Nanoparticle diameters and hydrodynamic diameters

Nanoparticle Diameters as Determined by TEM	
nanoparticle	average diameter (nm)
FA-PAA NP	9.42 +/- 0.5
Au seeded-Fe-PAA NP	11.01 +/- 0.5
DAN	32.5 +/- 1.8
Hydrodynamic Diameter as Determined by DLS	
nanoparticle	hydrodynamic diameter (nm)
Fe-PAA NP	45.56 +/- 1.0
DAN	53 +/- 1.2
*DLS was conducted in 100mM $NaHCO_3$ at 25° C	

To quantify the CSA bound to colloidal silver, a standard curve of integrated peak area vs CSA concentration was constructed using HPLC-ESI-TOF-MS (see Supporting Information). CSA was then displaced from the DAN surface and analyzed, again using HPLC-ESI-TOF-MS. The corresponding CSA concentration was determined to be 1.34 mg/L for a 500µL sample, or 4.01×10^{14} CSA molecules. Using ICP-OES it was determined the same 500µL sample contained roughly 5.27×10^{12} DANs, thus we conclude there are on average 76.1 CSA-124 molecules bound to each DAN. As the packing density and uniformity of the CSA-124 surfactant layer is critical to both particle stability and bacterial adhesion, future work will examine the optimization of this process.

Figure 2.7a shows a slightly inverse relationship between magnetization and temperature and that the magnetization of DANs at a physiological temperature is roughly 0.02 emu. Figure 2.7b is a hysteresis loop of the DANs. The DAN magnetization was measured as a function of applied field from 0 to ±90,000 Oe. As seen in the graph, the magnetization of DANs increases quickly with the applied field, tending toward saturation at fields > 5000 Oe. The maximum magnetization is roughly 12 emu/g NP, which is 54 emu/g Fe. This value is comparable to the iron oxide T2 contrast agents currently in clinical use; Feridex and Combidex have magnetizations of 45 emu/g Fe and 61emu/g Fe respectively [27].

The inset shows an expanded view of the low-field region of the magnetization in which a hysteresis is observed with a remnant magnetization, $M_r \sim 3.0$ emu/gm, and a coercive field, $H_c \sim 300$ Oe. The data suggest that the majority of the nanoparticles are paramagnetic and at least some subset of the nanoparticles have a ferromagnetic component to their magnetization. This is likely a result of the size distribution of the particles used in the iron core, some of which will be above the critical transition size from superparamagnetic to ferromagnetic, roughly 10nm.[55]

In Figure 2.8, a clear correlation is seen between nanoparticle concentration and MRI contrast, known as negative contrast. The paramagnetism of the NP's causes the relaxivity of nearby water molecules to drop, and a decrease in relaxivity results in a lower pixel intensity. Using ImageJ, the pixel intensity of each tube was measured

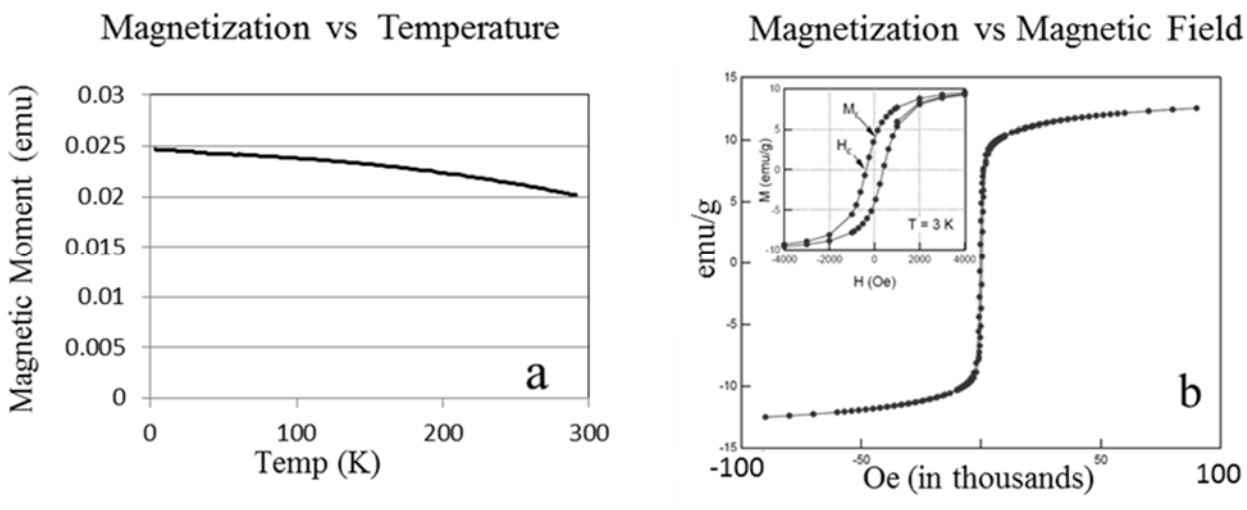

Figure 2.7 Graph (a) shows magnetization as a function of temperature. The hysteresis loop in graph (b) shows NP magnetization as a function of magnetic field.

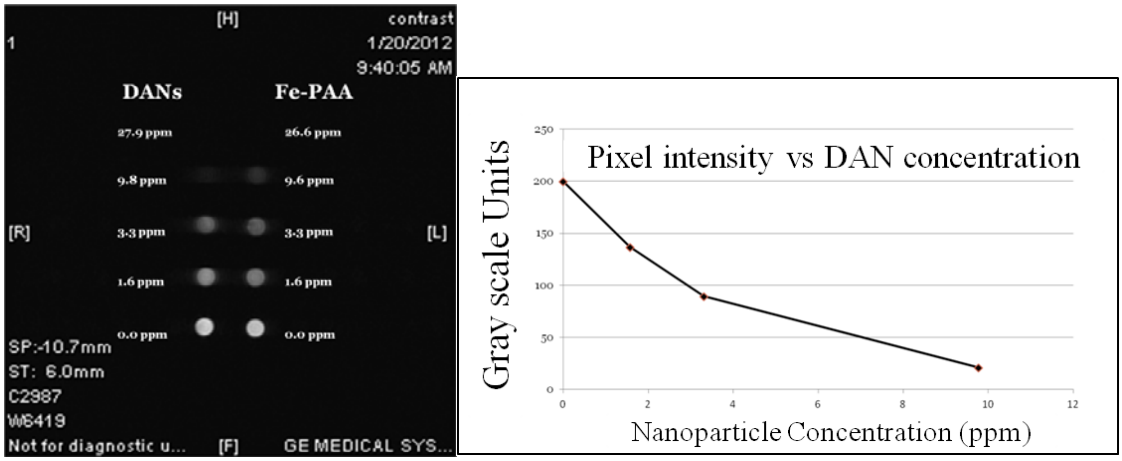

Figure 2.8 MRI of NPs dispersed in agarose at various concentrations (left). Graph of resulting pixel intensity for each sample concentration (right).

then plotted against particle concentration, as seen in Graph 1. On average, pixel intensity drops by 16.7 gray scale units for each additional ppm DAN. Figure 8 also shows the similar contrast of DANs and Fe-PAA NP indicating that the maghemite core is not

compromised by the formation of the silver shell. In fact, DANs seem as though they may have slightly increased contrast ability. This can potentially be explained by Dr. Vuong et.al. who postulate that surrounding a paramagnetic NP with a shell prevents it from directly coordinating with the select few neighboring water molecules but rather allows its effects to be distributed amongst a greater surface area and thus affecting a greater number of water molecules.[56]

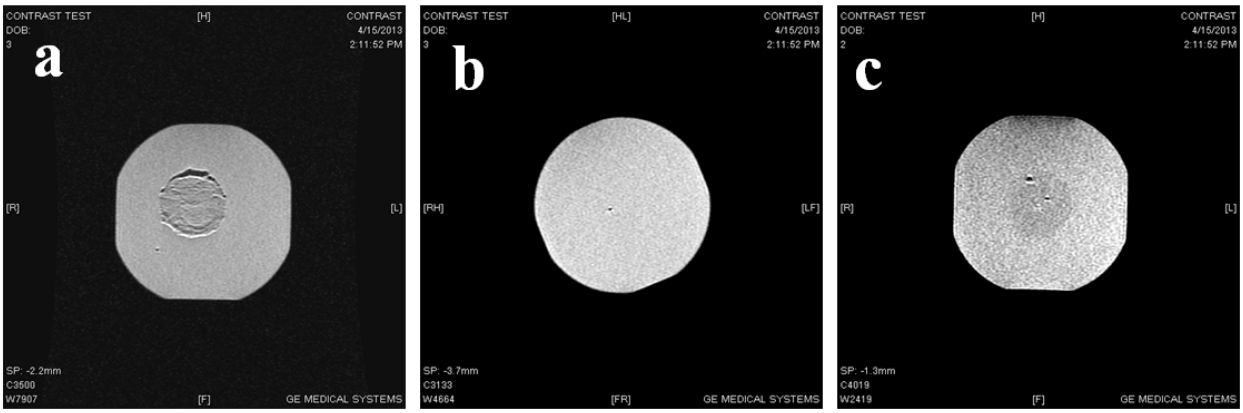

Figure 2.9 Magnetic Resonance Images of syringe filters suspended in agarose. Image "a" is a positive control, image "b" is a negative control, and image "c" is the treatment.

Determination of *in vitro* contrast of bacteria by DANs was assessed by exposing *S. aureus* to DANs, running this solution through a syringe filter, suspending this filter in a block of agarose, and imaging with MRI, seen in image Figure 2.9.c. Filter pores, 450nm, were chosen to be large enough to allow DANs to pass unhindered yet retain all bacteria. As a negative control, *S. aureus* was also exposed to DANs devoid of CSA-124, (Fe core with silver shell only) and filtered, image 2.9b. A positive control of total DAN capture using a 200nm filter that captured bulk of the DAN's on the filter media can be seen in Figure 2.9a. As anticipated, Figure 2.9a shows the greatest contrast, Figure 2.9b

shows no contrast and Figure 2.9c shows moderate contrast. This suggests that DAN attachment does occur, though the efficiency of the attachment is far below 100%. This may be caused by variation in the particle CSA -124 functionalization. As noted above the average functionality is 76.1 CSA/particle but distribution is currently unknown, as such large numbers of particles may have little or no CSA attached. The images also supports that DANS devoid of CSA do not adhere to the *S. aureus*, nor are they trapped in the filter. To ensure the attachment of CSA-124 to the NP surface did not affect filter permeability, fully conjugated DANs in DI were filtered and also resulted in no contrast (data not shown).

2.4 Conclusions

The results in this study suggest that the synthesis process described above successfully generates the desired iron containing, silver shell nanoparticle with a ceragenin monolayer surface functionalization. The FT-IR spectrums support the addition of a mercapto group to the Fe-PAA NP. ICP-OES demonstrated the final product is comprised of 76.64% silver, 22.75% iron, and 0.61% gold with ~8% total yield. Both TEM and DLS results demonstrate predictable growth of the particle with each additive process step. These results indicate that gold and silver were successfully deposited onto the Fe-PAA NPs, yielding a final nanoparticle of 32.474 $^{+}$/- 1.83 nm diameter and 53.053 $^{+}$/- 1.202 nm hydrodynamic diameter. Furthermore, these particles were shown to be predominantly paramagnetic and possess a strong magnetic moment of 54 emu/g Fe. These characteristics are representative of clinically adopted T2 MRI contrast agents, making DANs a good candidate for diagnostic use. MRI of DANs and maghemite core NPs at various concentrations suggest a 16.7 gray scale unit reduction in pixel intensity

for each ppm DAN. DANs have also demonstrated an ability to adhere and contrast *S. aureus in vitro*. The results presented in the report indicate DANs to be a potentially viable diagnostic contrast agent for deep tissue infection. Further work must be done to assess the cytotoxic qualities of DANs as well as their diffusion characteristics using a more advanced tissue phantom.

2.5 References

[1] M. Mahmoudi, S. Laurent, M.A. Shokrgozar, M. Hosseinkhani, ACS Nano, 5 (2011) 7263-7276.

[2] J.S. Kim, E. Kuk, K.N. Yu, J.H. Kim, S.J. Park, H.J. Lee, S.H. Kim, Y.K. Park, Y.H. Park, C.Y. Hwang, Y.K. Kim, Y.S. Lee, D.H. Jeong, M.H. Cho, Nanomed.-Nanotechnol. Biol. Med., 3 (2007) 95-101.

[3] S.S. Agasti, A. Chompoosor, C.C. You, P. Ghosh, C.K. Kim, V.M. Rotello, J. Am. Chem. Soc., 131 (2009) 5728-+.

[4] J. Nakanishi, H. Nakayama, T. Shimizu, H. Ishida, Y. Kikuchi, K. Yamaguchi, Y. Horiike, J. Am. Chem. Soc., 131 (2009) 3822-+.

[5] D.P. O'Neal, L.R. Hirsch, N.J. Halas, J.D. Payne, J.L. West, Cancer Lett., 209 (2004) 171-176.

[6] K. Cheng, T.S. Li, K. Malliaras, D.R. Davis, Y.Q. Zhang, E. Marban, Circ.Res., 106 (2010) 1570-U1554.

[7] B. Chertok, B.A. Moffat, A.E. David, F.Q. Yu, C. Bergemann, B.D. Ross, V.C. Yang, Biomaterials, 29 (2008) 487-496.

[8] K.T. Yong, Y. Sahoo, M.T. Swihart, P.N. Prasad, Colloid Surf. A-Physicochem. Eng. Asp., 290 (2006) 89-105.

[9] J.B. Jackson, N.J. Halas, J. Phys. Chem. B, 105 (2001) 2743-2746.

[10] S. Pal, Y.K. Tak, J.M. Song, Appl. Environ. Microbiol., 73 (2007) 1712-1720.

[11] X. Chen, Gambhir, Sanjiv, Accounts of Chemical Research 44 (2011) 841-1134.

[12] S.e.a. Narayanan, Applied Material Interfaces, ASAP (2011).

[13] H.B. Na, I.C. Song, T. Hyeon, Adv. Mater., 21 (2009) 2133-2148.

[14] C. Schweiger, P. Gil, W. Parak, T. Kissel, J. Control. Release, 148 (2010) E67-E68.

[15] L. Babes, B. Denizot, G. Tanguy, J.J. Le Jeune, P. Jallet, J. Colloid Interface Sci., 212 (1999) 474-482.

[16] R.O. Becker, Metal-based drugs, 6 (1999) 311.

[17] W.K. Jung, H.C. Koo, K.W. Kim, S. Shin, S.H. Kim, Y.H. Park, Appl. Environ. Microbiol., 74 (2008) 2171-2178.

[18] E. Katz, I. Willner, Angew. Chem.-Int. Edit., 43 (2004) 6042-6108.

[19] P. Ghosh, G. Han, M. De, C.K. Kim, V.M. Rotello, Adv. Drug Deliv. Rev., 60 (2008) 1307-1315.

[20] D.S. Seferos, A.E. Prigodich, D.A. Giljohann, P.C. Patel, C.A. Mirkin, Nano Lett., 9 (2009) 308-311.

[21] D.F. Emerich, C.G. Thanos, Biomol. Eng., 23 (2006) 171-184.

[22] K. Leszczynska, A. Namiot, D.E. Fein, Q. Wen, Z. Namiot, P.B. Savage, S. Diamond, P.A. Janmey, R. Bucki, BMC Microbiol., 9 (2009).

[23] R. Bucki, A.G. Sostarecz, F.J. Byfield, P.B. Savage, P.A. Janmey, J. Antimicrob. Chemother., 60 (2007) 535-545.

[24] K. Leszczynska, A. Namiot, K. Cruz, F.J. Byfield, E. Won, G. Mendez, W. Sokolowski, P.B. Savage, R. Bucki, P.A. Janmey, J. Appl. Microbiol., 110 (2011) 229-238.

[25] M.M. Ling, K.Y. Wang, T.S. Chung, Ind. Eng. Chem. Res., 49 (2010) 5869-5876.

[26] M. Brust, M. Walker, D. Bethell, D. Schiffrin, R. Whyman, Journal of the Chemical Society, Chemical Communications, 1994 (1994) 801-802.

[27] M. Lattuada, T.A. Hatton, Langmuir, 23 (2007) 2158-2168.

[28] Z. Grabarek, J. Gergely, Anal. Biochem., 185 (1990) 131-135.

[29] P. Tengvall, E. Jansson, A. Askendal, P. Thomsen, C. Gretzer, Colloid Surf. B-Biointerfaces, 28 (2003) 261-272.

[30] C. Merlic, in: UCLA (Ed.) WebSpectra, Los Angeles, 2000.

[31] S . Dutz, R. Hergt, J. Mürbe, R. Müller, M. Zeisberger, W. Andrä, J. Töpfer, M.E. Bellemann, Journal of Magnetism and Magnetic Materials, 308 (2007) 305-312.

CHAPTER 3. SELECTIVE ANTIMICROBIAL: SILVER NANOPARTICLE WITH SELF ASSEMBLING CERAGENIN MONOLAYER

Brief Summary: This report explores silver nanoparticles conjugated to ceragenin, or cationic steroidal antimicrobials (CSA-SNPs), as a gram-positive selective antimicrobial. Herein, CSA-SNPs are characterized using TEM, DLS, zeta potential, and HPLC-ESI-TOF-MS. The antimicrobial properties and microbial selectivity are determined through MIC/MBC studies, confocal imaging, MATLAB image analysis, and video monitored interactions between bacteria and CSA-SNPs using laser trapping techniques. Cytotoxicity is also determined via live/dead staining and flow cytometry. Average particle size as determined through TEM analysis and hydrodynamic diameter determined via DLS are 63.5 +/- 38.8 nm and 102.233 +/- 2.3 nm respectively. The zeta potential of the SNP before and after CSA attachment is -18.23 mV and -8.34 mV. MIC/MBC data suggests CSA-SNPs are eight times more effective against *Staphylococcus aureus* than SNPs alone. Furthermore, MATLAB analysis of confocal imaging found that 70% of CSA-SNPs are within 2 μm of *S. aureus* whereas this percentage falls to below 40% with respect to *Escherichia coli.* These results are bolstered further by laser trapping experiments demonstrating selective adherence ofCSA-SNPs conjugates with bacterial strains. Cytotoxicity studies of CSA-SNPs against 3T3 fibroblasts indicate 50% cell viability at 50 ppm.

3.1 Introduction

A significant source of difficulty in treating infections is the broad spectrum activity of state-of-the-art antibiotics. In the attempt to eliminate pathogenic microbes, many antibiotic treatments also kill or inhibit the natural microbial fauna [57]. Natural microfauna aid in acquiring nutrients and provide protection against colonization by pathogenic microorganisms[57]. When these natural bacterial populations become compromised, opportunistic pathogens such as *Clostridium difficile*, *Candida ablicans*, and *Staphylococcus aureus* can impair post-treatment recovery or require additional treatment [57-60]. Selective antimicrobial agents aim to treat infections while leaving native microbiome unaffected.

Advances in the chemistry of inorganic nanoparticles, has lead to a rapid increase in the number of types and potential uses for nanoparticles [10, 61-63]. Nanoparticles can be facilely manufactured from a large variety of materials, as well as in a variety of shapes, sizes, number of layers, and surface chemistries. An area of particular interest is the use of nanoparticles as a vehicle for the delivery of drugs [62]. Nanoparticles offer a high surface area-to-volume ratio allowing high drug carrying capacity and additionally nanoparticles can be targeted to infected tissues and regions to deliver sustained drug treatment [18, 64, 65]. Ligands attached to nanoparticles are also less prone to degradation than when free in solution [18]. Additionally, for amphiphillic molecules with thiol groups it is thermodynamically advantageous to self-assemble on noble metals such as silver or gold [66, 67]. Particles less than 200 nm are more likely to remain in circulation *in vivo* than larger nanoparticles [18]. Taken together this ability to

manipulate the composition, morphology and surface chemistry of nanoparticles make them excellent candidates for selective antimicrobials.

Silver has long been known to have antimicrobial properties and correspondingly, silver nanoparticles (SNPs) and other silver nanomaterials have been shown to posses similar antimicrobial properties [61, 68-72]. Silver is used as an antimicrobial in several devices including bandages, antibacterial gels, and catheters [73]. Silver impacts microbial systems through several mechanisms resulting in the disruption of many crucial cell functions such as cell wall and nucleic acid synthesis, translation, protein structure, and membrane ion pumps. Without these functions, cell division inhibition or death often occurs. This combination of potent antimicrobial activity and limited cytotoxicity makes SNPs potentially favorable as an alternative to traditional antibiotics as a treatment for infections.

Natural cationic peptides display potent antimicrobial properties with low rates of resistance and varying levels of selectivity. However, many are vulnerable to protease activity, limiting their usefulness as an antibiotic in vivo [74, 75]. Ceragenins, also called cationic steroid antimicrobials (CSAs), are synthetic molecules designed to imitate the activities of these naturally occurring antimicrobial peptides [76]. CSAs have been demonstrated as effective antimicrobials against drug-resistant strains of *Pseudomonas aeruginosa* [77], *Helicobacter pylori* [78], *Staphylococcus aureus* [79], and periodontic bacteria such as *Streptococcus mutans* and *Porphyromonas* species [80]. A novel ceragenin, CSA-124, has been synthesized with a terminal thiol group allowing for specific covalent bonding to noble metals.

Herein we demonstrate the synthesis of a CSA-124 conjugated SNP (CSA-SNP) with improved antimicrobial activity and physical selectivity for *Staphylococcus aureus*. The particles composition and physical properties are explored through TEM, DLS, ICP-OES and LC-ESI-MS. The antimicrobial efficacy is demonstrated with standard MIC/MBC assays and mammalian cytotoxicity of the CSA-SNP constructs are quantified using live/dead staining and flow cytometry. Physical selectivity is demonstrated both qualitatively and quantitatively through confocal microscopy and laser trapping analysis.

3.2 Methods and Materials

Materials

SmartSilver™AS was purchased from NanoHorizons Inc (Bellefonte, PA). Dialysis membranes (10,000 Da) were ordered from Sigma-Aldrich®. TEM grids and paraformaldehyde (16%) were obtained from Electron Microscopy Sciences (Hatfield, PA). The Acclaim® Mixed-Mode HILIC-1 normal phase LC column was ordered from ThermoScientific (Logan, Utah). For cell culture, DMEM-RS™, Trypsin (0.25% (1X solution), and DPBS/modified(1X) are HyClone® products and also ordered through ThermoScientific. Sytox® Red dead cell stain was purchased from Molecular Probes™ by Life Technologies Corporation ™ and Live BacLight™ Bacterial Gram Stain Kit was purchased from Invitrogen™ Molecular Probes™ (Eugene, Oregon). CSA-124 was prepared by functionalizing a leac ceragenin, CSA-13, with a thiol group on a short PEG tether. Synthetic details for CSA-124 will be reported elsewhere. All other chemicals were used as received unless otherwise noted. For bacterial culture Mueller Hinton Broth, and Nutrient Agar, pH6.0 with 0.8%NaCl was purchased from Himedia®/VWR™, and

Mannitol Salt Agar was purchased from acumedia®/Neogen® corporation Lansing, Michigan.

Methods

Conjugating Silver Nanoparticles with CSA-124

An appealing quality of the CSA-SNPs is the easy of conjugation. A four mL suspension of SNPs in DI water at 300ppm was mixed with 50µL CSA-124 in DI water at 0.2 mM. This solution was allowed to react overnight at room temperature, then purified in dialysis sacks, pore size 12,000 Da MWCO, for 24 hours changing water 3 times.

Dynamic Light Scattering (DLS):

Hydrodynamic diameters were measured using a Malvern Zetasizer nano series (Worcestershire, UK). NP samples from various stages of synthesis were diluted to roughly 0.02 ppm in $NaHCO_3$/DI (100 mM) then filtered using a Thermo Scientific Nalgene 0.2 µm surfactant-free cellulose acetate membrane. Samples were measured in Malvern ZEN0040 disposable cuvettes at 25˚ C. In determination of zeta potential, NPs were suspended in DI, filled a Zetasizer nano series folded capillary cell, and also measured using a Malvern Zetasizer nano series (Worcestershire, UK) at 25 ˚ C.

Transmission Electron Microscopy (TEM):

The TEM images were obtained using a JOEL 2011 ™ (Tokyo, Japan). Nanoparticle samples were diluted to roughly 25 ppm in DI water and 5 µL was applied

to an Electron Microscopy Sciences carbon film 400 square mesh copper grid and allowed to air dry. Images were taken at 150,000X. TEM images were analyzed using Metamorph Advanced software. The diameters of 25 nanoparticles of each type were measured using digital calipers and statistical significance was determined using a one sample t-test.

CSA Quantification:

A five point standard curve, $R^2 = 0.9942$, was constructed by comparing known concentrations of CSA-124 dissolved in 25% $^{v}/_{v}$ acetonitrile (ACN) in DI to the integrated area of its HPLC-ESI-TOF-MS peak. CSA-124 was displaced from the SNP and run through HPLC-ESI-MS/MS, then quantified by comparison to this standard curve. To remove CSA from the SNP, 5.5 µL DL-Dithiothreitol (DTT) was added to 500 µL CSA-SNPs and allowed to react for one hour at 37° C. The DTT displaces the CSA from the SNP surface resulting in DTT-SNPs and a solution of CSA and unreacted DTT. Particles were then separated via centrifugation for 15 minutes at 12xg. The supernatant was removed and concentrated from 500 µL to 250 µL by vacufugation and 250 µL of ACN/DI (50% v/v) was then added to the solution bringing the final solution to 25% ACN, mirroring the standard curve solution. The samples were then analyzed by HPLC-ESI-TOF-MS (Agilent 1200 with a binary pump/Agilent ESI TOF 6210 PALO ALTO, CA). The LC column used was a normal phase Acclaim® Mixed-Mode HILIC-1, 3µm Analytical (2.1 x 150mm). Samples and standards were injected at 2 µL. The first mobile phase was 90% ACN in water with 0.1% formic acid while the second mobile phase was water with 0.1% formic acid. The ESI parameters used are as follows: nitrogen

temperature 325° C, nitrogen flow 5 L/min, and nebulizer pressure 20 psi. The DTT-SNP pellet obtained from the previously mentioned centrifugation was quantified by ICP-OES.

Cytotoxicity Analysis

Murine 3T3 fibroblast cells were seeded onto 12-well plates in 500 µL of growth medium (DMEM, 10% FBS) and allowed to grow for 48 hours till 80% confluent. The medium was then replaced with 600 µL medium containing incremental concentrations of CSA-SNPs. Live controls received 600 µL of the growth medium containing no CSA-SNPs. Dead controls received 600 µL of growth medium as well as 150 µL of 70% ethanol solution. The cells were incubated at 37 °C in 5% CO_2.

The 3T3 cells were incubated in the CSA-SNP medium for 24 hours. Then the medium was removed and collected. The cells were lifted from the 12- well plates using Trypsin and collected in combination with the previously removed media. The cells were then separated through centrifugation and resuspended in 1 mL phosphate-buffer saline (PBS; -Ca, -Mg). The cells were stained for viability using Sytox Red, 1 µL for 15 minutes, then separated via centrifugation, and fixed in 350 µL of 1% polyformaldehyde (PFA) solution. The live and dead counts were evaluated using flow cytometry.

Hemolytic Characterization

The hemolytic properties of CSA-SNP were assessed using the ASTM E2524-08 protocol Standard Test Method for Analysis of Hemolytic Properties of Nanoparticles.

This test evaluates the effect CSA-SNPs have on the integrity of red blood cells by in vitro exposure and quantification of hemoglobin released. First hemoglobin standards were made covering a range from 0.025 to 0.8 mg/L and a standard curve was generated. Hemoglobin is oxidized to methemoglobin by ferricyanide in the presence of alkali. This concentration can be determined by measuring absorbance at 540 nm. Blood was diluted in PBS ($-Ca^{2+}/Mg^{2+}$), to hemoglobin concentration of 10 mg/mL. In a test tube 700 µL PBS, 100 µL diluted blood solution, and 100 µL CSA-SNP solution were mixed and placed on an orbital shaker for 30 minutes. The samples were then placed in a water bath set to 37 ˚C for 3 hours and 15 minutes. Next samples were centrifuged for 15 minutes at 800x*g* and the supernatant was collected. 100 µL of supernatant was added to a 96 well plate along with 100 µL cyanmethemoglobin reagent, covered, gently shaken, allowed to react for 10 minutes, then its absorbance at 540 nm was measured on a plate reader. This absorbance was compared to the standard curve to determine hemoglobin concentration. This concentration divided by the total hemoglobin concentration of the diluted blood solution yields percent hemolysis. A 10% Triton X solution was used as the positive control to determine total blood hemoglobin. Each sample was run in triplicate and known standards were run with each sample to ensure they matched up properly with the standard curve.

Brightfield Imaging of Cell Morphology.

To qualitatively asses cell heath after CSA-SNP exposure, 3T3 fibroblasts were seeded with DMEM/10%FBS into 9 wells of a MULTIWELL™ 12 well tissue culture treated plate and incubated at 37˚ C and 5% CO_2 until 50% confluent, about two days.

The media was removed from all wells. Three of these wells were exposed to 600 µL DMEM/10%FBS, three received a 600 µL solution of CSA-SNPs in DMEM/10%FBS at 15ppm, and three wells received 600 µL solution of CSA-SNPs in DMEM/10%FBS at 37ppm. Samples were incubated 24 hours, again at 37˚ C and 5% CO_2. Wells were imaged using a Nikon eclipse TS100 brightfield microscope (Melville, NY), PHOTOMETRICS® CoolSNAP camera (Tucson, AZ), and MetaMorph® Advanced image analysis software.

Minimum Inhibitory Concentration & Minimum Bactericidal Concentration

The minimum inhibitory concentration (MIC) was determined using a protocol modified from that of J. M. Andrews[81]. Briefly, the inoculum was prepared by mixing one loop of the desired bacteria in 10 mL of Mueller Hinton Broth (MHB), which was then incubated at 37˚ C overnight. This inoculum was found to be ~1.6 x 10^8 cfu/mL by plating serial dilutions. For testing, inoculum was used promptly that day and diluted to 1 x 10^6 cfu/mL. Alternatively, a McFarland Standard could be used in inoculum dilution[82]. In preparation of the serially diluted 96 well plate, 100 µL of pure MHB was added to each well. Next 100 µL of the antimicrobial solution, CSA-SNPs mixed in phosphate buffered saline (PBS) to 480 ppm, was added to the first well of each row. Then using a multichannel pipette set to 100 µL, the CSA-SNP/MHB solution was serially diluted across, thus making each consecutive well 50% the concentration of the well preceding it. At this time 100 µL of the prepared inoculum was added to each well and the plate was incubated overnight. The MIC is defined as the most dilute concentration of an antimicrobial that will inhibit visible growth of a microbe after

overnight incubation[81, 82]. Each row should contain a live control/negative control, i.e. a well that contains no antimicrobial. Each row should also include a well consisting of only the pure MHB. This well should remain clear after incubation, thus ensuring that the MHB was not contaminated at any point in the study. These two controls also serve as a means of comparison for the treatment wells, one representing uninhibited growth and the other representing no growth. Minimum bactericidal concentration (MBC) was then determined using methods established by LJ.de Nooijer and Wallert and Provost Lab[83, 84]. To each well of the 96 well plate with a concentration equal to or greater than that of the MIC, 40 μL, 5 ppm 3-(4,5-Dimethyl-2-thiazolyl)-2,5-diphenyl-2H-tetrazolium bromide (MTT) was added and the plate was incubating 4 hours at 37˚C [83]. Any indication of color change from yellow to purple precipitate indicates viable bacteria. This can be confirmed by adding 150 μL MTT solvent to each well and measuring absorbance at 590nm; deviation in absorbance from a no bacteria control will indicate viable bacteria are present. The most dilute concentration of antimicrobial agent that results in no viable bacteria is the MBC [85]. All trials were run in triplicate.

Confocal Imaging

Spatial selectivity of the CSA-SNPs to *S. aureus* was visualized using Leica Microsystems DM IRE 2 confocal microscope system and corresponding software. *E. coli* and *S. aureus* were cultured in Mueller-Hinton nutrient broth for 24 hours at 37°C. After incubation, *E. coli* and *S. aureus* was diluted to roughly $1x10^7$ cfu/mL. Dilutions were into sterile bacterial broth. Five hundred μL of each dilution was then placed into the same well of a Lab-Tek® II Chambered #1.5 German Coverglass System. The co-

culture of bacteria was allowed to affix to the slide for 1 hour undisturbed. The solution was then removed. Next, the co-culture was exposed to SNP-CSA diluted into PBS+ Ca^{2+} and Mg^{2+} at 24 mg L^{-1}. The co-culture was exposed to the CSA-SNP on a wobble plate. This solution was removed after 30 minutes. The well was rinsed with 500 µL of PBS+ to remove excess nanoparticles. After the rinse was removed, the co-culture was stained with Life Technologies™ LIVE BacLight™ Bacteria Gram Stain Kit. In accordance with manufacturer's protocol, the stain was prepared by mixing 1.5 µL of BacLight component A (SYTO® 9) and 1.5 µL of component B (hexidium iodide) into 500 µL of PBS - Ca^{2+} and Mg^{2+}. The bacteria were allowed to stain for 15 minutes in the dark, and then imaged using Leica Microsystems DM IRE 2 confocal microscope system and software.

Image Analysis

Quantitative analysis was performed on the confocal and TEM images using the Image Processing Toolbox in MATLAB (MathWorks, Natick, MA). For TEM analysis: grayscale images were converted to binary images with a threshold calculated by Otsu's method [28]. After comparison with the original images, thresholds were manually adjusted if necessary. Binary morphological operations were performed to identify nanoparticles, which were then counted as groups of connected pixels. Finally, effective diameters were estimated given a known area of pixels for each nanoparticle and assuming a circular cross-section; n=397 nanoparticles.

For quantitative confocal analysis, images from each imaging channel were read into MATLAB. A threshold was again calculated by Otsu's method [28] and modified

manually after comparison with the overlay of the three channels (due to differential uptake of each stain, cell morphology was used when necessary to aid in manual threshold determination). Next, the centroids of isolated objects (*S. aureus* cells, *E. coli,* and silver nanoparticles) in each channel were identified. Using the two-dimensional distance formula, the distance from the centroid of a single nanoparticle to the centroid of every *S. aureus* and *E. coli* was calculated; the minimum distance of those calculated for *S. aureus* and *E. coli* represents the closest of *S. aureus* and *E. coli*, respectively, to that nanoparticle. This process was repeated for each nanoparticle in the image. Statistical analysis, specifically student's T-Test for significance and Ripley's K-function [29] for clustering, were performed.

Optical Trapping

The basic design of the optical trap setup can be found in Supplemental Information. The instrument (MMI CellManipulator, MMI, Zurich, Switzerland) was fabricated to work as an optical trapping system with force measurement capabilities. The optical trapping laser used was an 8 W Nd: YAG (yttrium aluminum granet) laser emitting light at a wavelength on 1070nm. The laser beam used was expanded to fit the back aperture of the microscope objective. The objective used was a 100X plan fluro objective (Nikon Instruments). A galvanometer was used that could create up to 20 individual traps simultaneously using a time-sharing mode. The instrument was designed as an optical trapping system using a Nikon TE2000 for imaging. Also, for this study CSA-NPs were synthesized of polystyrene beads functionalized with a colloidal silver shell and CSA-124. These particles share the same surface chemistry as the CSA-SNP

but are larger, roughly 1micron. This is necessary as optical capture is not feasible for smaller objects.

A glass slide was passivated with dried milk, and a diluted sample of CSA-MP and *S. aureus* was placed on the surface. The slide was then sealed with a glass coverslip and parafilm. The slide was then placed under 100x oil immersion objective and the laser turned on. Two traps were created, one for a single bacteria and another for a CSA-MP nanoparticle. The laser power was adjusted to about 30% to minimize potential spurious laser interactions and heating. The trap containing the bacteria was slowly moved to approach the *S. aureus* to eventual contact, as indicated by slight displacement of both. In this series of measurements the staph/CSA-NP adduct was annealed about 2 seconds before moving the traps apart. The same procedure was followed with identical beads that did not contain CSA-124. Results reported are based on an average of 200 trials repeated over 80 sets of independently prepared microscope.

3.3 Results and Discussion

Nanoparticle size was determined through TEM image analysis and DLS. These results are reported in Table 1. As expected the hydrodynamic diameter determined via DLS is greater than the diameter determined via TEM due to the presence of solvated surfactant on the particle surface. Also of note is that the hydrodynamic diameter increased as the positively charged CSA-124 molecules were added to the system, indicating self-assembly on the nanoparticle surface. While size of CSA-SNPs is not critical in these experiments, it is relevant to colloidal stability and *in vivo* biocompatibility. Larger particles are more likely to settle from solution potentially

irreversibly aggregating and increasing apparent size. Also, nanoparticles possessing a diameter greater than 200nm are more prone to activate the complement system and thus be cleared from the circulatory system [31]. Nanoparticles with a diameter under 100nm are capable of penetrating blood vessel pores and NPs under 20nm can access interstitial spaces[18]. This characteristic has been termed the enhanced permeability and retention (EPR) effect [3, 19].

Table 3.1. Nanoparticle characterization

Parameter	HPC-SNP	CSA-SNP
SNP diameter via TEM analysis (nm)		63.5 +/- 38.8
Hydrodynamic diameter (nm)	81.9 +/- 9.4	102.233 +/- 2.3
Zeta potential (mV)	-18.23 +/- 0.83	-8.34 +/- 1.05

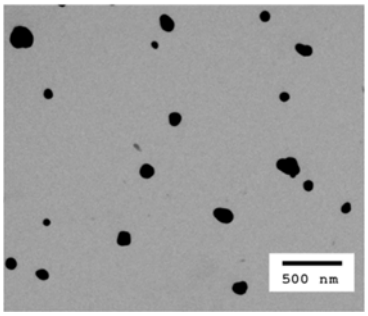

Figure 3.1 TEM of CSA-SNP

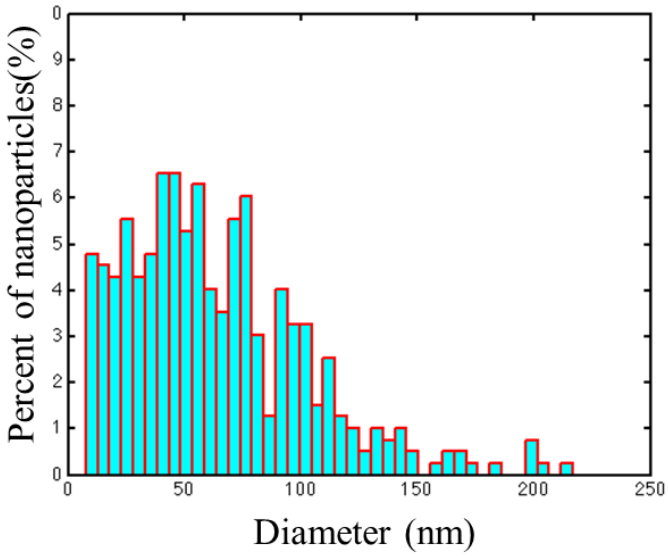

Figure 3.2 Histogram of CSA-SNP size as determined by TEM image analysis

As expected, the nanoparticle gains positive charge after the addition of CSA, a *cationic* steroidal antimicrobial, and purification of the resulting particles. This data supports the fact that CSA was successfully conjugated to the nanoparticle surface. It is also relevant because the nature of the surface charge also effects the nanoparticles' *in vitro* and *in vivo* interactions. Particles with a moderately neutral charge will be more likely to agglomerate resulting in shorter shelf lives, a lower solubility threshold, and an increased probability of removal from *in vivo* circulation [30]. Once in the body, nanoparticles are susceptible to opsonization, recognition, and removal by the mononuclear phagocyte system (MPS). In general, neutral to negatively charged nanoparticles with hydrophilic polymer surfaces exhibit prolonged circulation times [31].

An appealing quality of the CSA-SNP is the ease of noble metal nanoparticle conjugation. CSA-124 has been specifically synthesized with a thiol-terminated polyethylene glycol side chain which favorably binds to noble metals. The

SmartSilverAS silver nanoparticles, from this point referred to as SNPs, used for this procedure are stabilized with hydroxypropyl cellulose (HPC), which provide the NPs with high solubility in aqueous and organic alcohol sovent systems. and biocompatibility. Because CSA-124 has greater thermodynamic and steric stability than HPC on the surface of the SNPs, CSA-124 spontaneously displaces a portion of the HPC molecules.

For the quantification of CSA-124 bound to the SNP surface, a standard curve was first constructed of integrated peak area vs known CSA concentration using HPLC-ESI-TOF-MS (Supporting Information). The CSA was displaced from the SNP surface using DTT, the particles were separated by centrifugation, and analyzed using HPLC-ESI-TOF-MS. The corresponding CSA concentration was determined to be 1.5 mg/L for a 500µL sample, or 4.52×10^{14} CSA molecules. Using ICP-OES and estimates of particle size from TEM it was determined the same 500µL sample contained roughly 1.32×10^{11} SNPs, thus we conclude there are on average 3,424 CSA-124 molecules bound to each SNP. Future work will concentrate on optimizing this parameter.

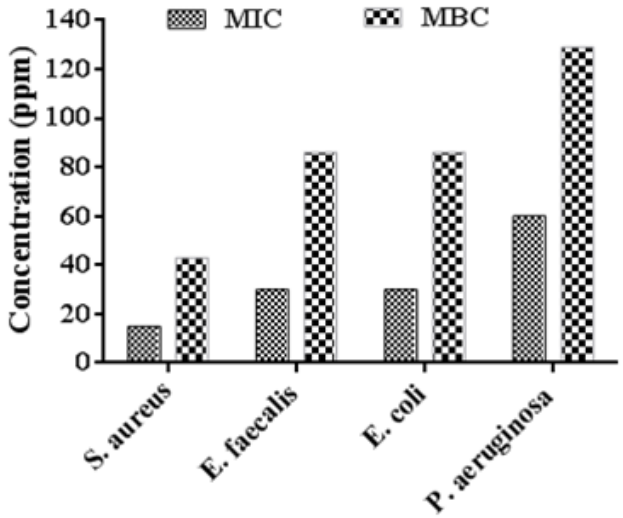

Figure 3.3 MIC and MBC of CSA-SNP against various bacteria

The antimicrobial results for the minimum inhibitory concentration (MIC) and minimum bactericidal concentration (MBC) are reported here in figure 3.3. As the graph indicates, CSA-SNPs are more efficacious against *S. aureus*, MIC 15 ppm, somewhat less effective against *E. faecalis* and *E. coli*, MIC 30, and least effective against *P. aeruginosa*, MIC 60. The data also suggests that CSA-SNP expresses higher selectivity toward gram positive bacteria, *S. aureus* and *E. faecalis*, than gram negative bacteria, *E. coli* and *P. aeruginosa*. This could be due in part to electrostatic attraction between the cationic steroidal antimicrobials and the negatively charged peptidoglycan, of which gram positive bacterial express in much greater quantities[86]. Ruparelia *et al*. determined the average MIC of SNPs against four different strains of E. coli and three different strains of *S. aureus*[87]. The average MIC against both *E. coli* and *S. aureus* was reported to be 120 ppm, making CSA-SNP's roughly 8 times more effective against *S. aureus* and 4 times more effective against *E. coli*. Our own determination of the MIC of SNPs was obtained using the same protocol as above and found to be roughly 250 ppm for both *S. aureus* and *E. coli*. Selectivity of CSA-SNPs was further explored through confocal imaging.

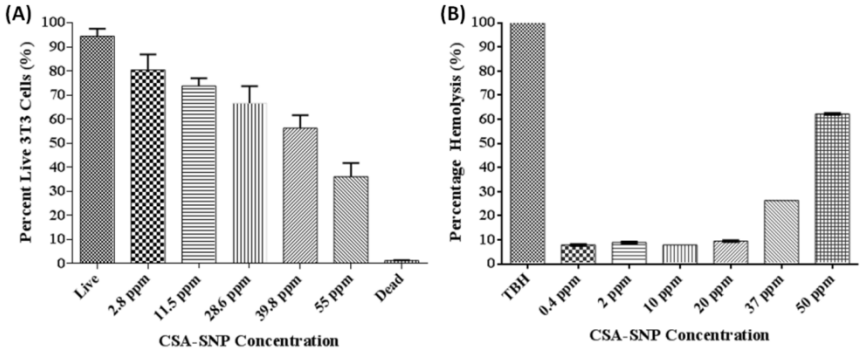

Figure 3.4 (A) Cytotoxicity of CSA-SNPs. (B) Hemolytic character of CSA-SNPs

The concentration dependent toxicity of CSA-SNPs to mouse 3T3 fibroblasts was determined by cell treatment followed by flow cytometry, and is presented in figure 3.4. The CSA-SNPs show very limited toxicity below 39.8 ppm, and reach the 50% viability threshold at ~50 ppm. Differences between neighboring columns were not found to be significant by one-way ANOVA with Bonferroni's posttest ($p < 0.05$), however all non-neighboring columns are significantly different. The hemolytic assay shows nearly identical results with increasing hemolysis at 37.5 ppm and slightly over 50% hemolysis occurring at 50 ppm. All values calculated in the hemolysis assay are significantly different except 0.4ppm vs 10ppm as determined by one-way ANOVA with Bonferroni's posttest ($p < 0.05$). These findings suggest a ~ 3.3 fold difference between MIC and EC_{50tox} for *S. aureus* and 3T3 cells respectively. Simultaneous testing of SNPs alone showed little cytotoxicity up to 200 ppm. This result is supported by the work of Jain *et al*. who reported that the IC_{50} for SNPs against Hep G2 cells to be 251 ppm. These findings suggest that CSA-SNPs are roughly 5 times more toxic to 3T3 cells than SNPs alone [88].

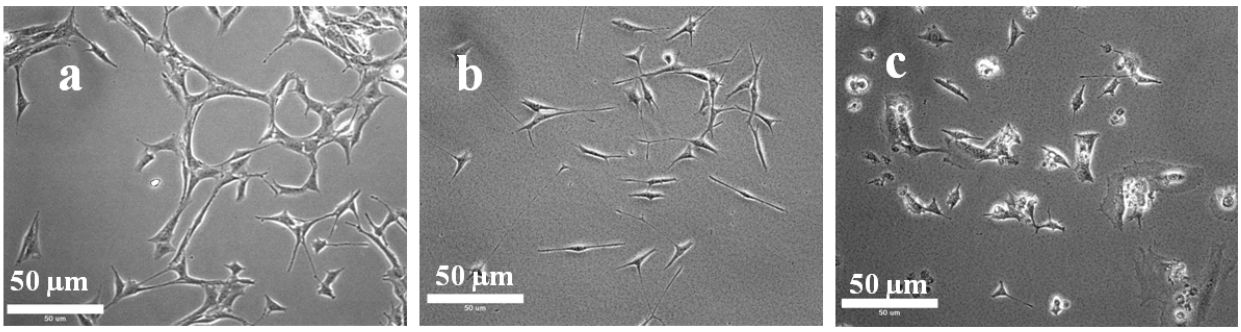

Figure 3.5 Brightfield images of 3T3 fibroblasts; "a" received 0 ppm CSA-SNP, "b" received 15 ppm CSA-SNP, and "c" received 37 ppm CSA-SNP

The cytotoxic effects of CSA-SNPs were also qualitatively assessed via brightfield imaging. In Figure 3.5a the typical spindle morphology of healthy 3T3 fibroblast cells can be seen. Figure 3.5b, representing the MIC of *S. aureus* at 15ppm CSA-SNP, the cells appears to have slightly reduced size but retain their characteristic spindle morphology. CSA-SNP at 37 results in stark contrast in cell morphology indicative of cytotoxicity. These results are consistent with those from the hemolysis and flow cytometry studies.

Qualitative image analysis of the confocal overlays (Figure 3.6) suggests that the CSA-SNPs are distributed spatially closer to *S. aureus* cells than *E. coli*. Analysis of these images provides the closest *S. aureus* and *E. coli* to each SNP; histograms and simple statistics are shown in Figure 3.7 and Table 3.2, respectively.

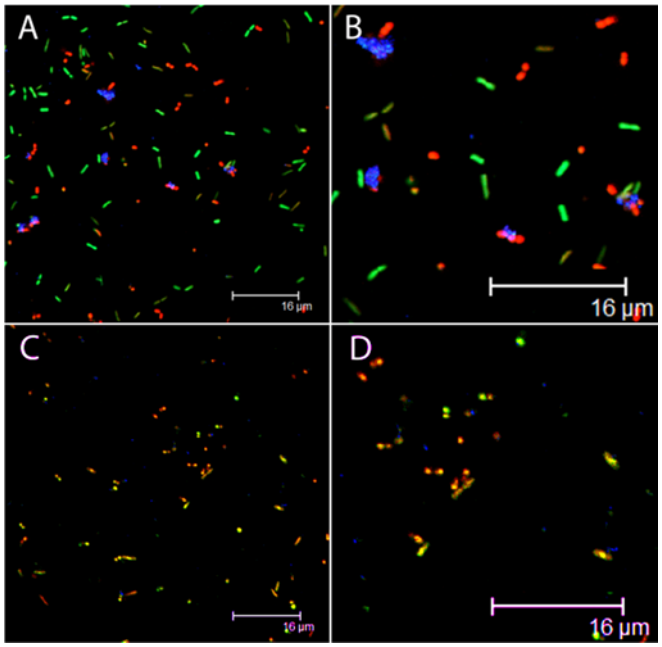

Figure 3.6 Confocal imaging of *S. aureus* (red), *E. coli* (green), and nanoparticles (blue). Images "B" and "D" are enlarged segments of "A" and "C" respectively. The NPs in "A" and "B" are CSA-SNPs while the NPs in "C" and "D" are SNPs

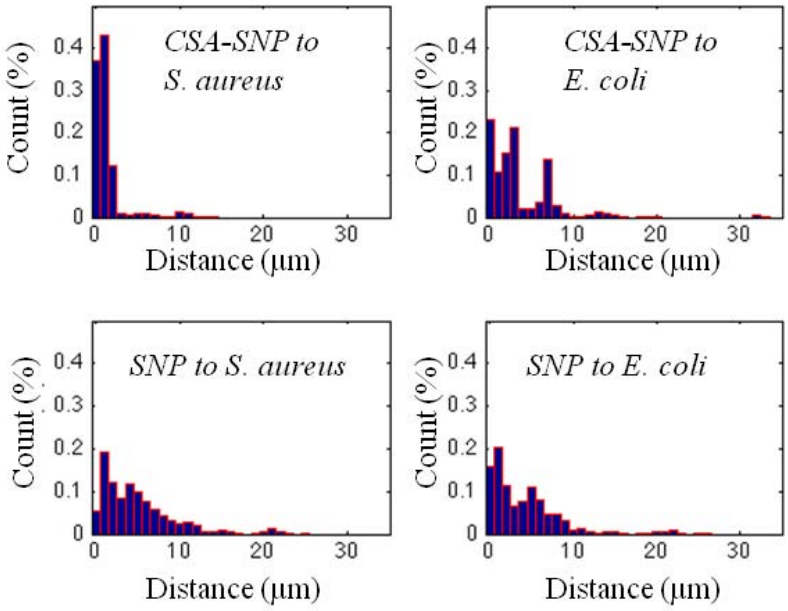

Figure 3.7 Histogram of distances: experimental (top), negative control (bottom), SNPs to *S. aureus* (left), and *E. coli* (right).

Table 3.2 Statistics from quantitative image analysis

Samples	Ave. Distance from NP to Cell (μm)
CSA-SNP to *S. aureus*	1.283
CSA-SNP to *E. coli*	3.4886
SNP (neg. control) to *S. aureus*	4.8638
SNP (neg. control) to *E. coli*	3.9910

Table 3.2 illustrates the distribution of distances for both experimental and negative control groups. The difference in average distance between CSA-SNP and *S. aureus* vs CSA-SNP and *E. coli* is statistically significant, as is the difference in average distance between the CSA-SNP treatment samples and the SNP negative control samples.

More than 70% of the CSA-SNPs are within 2 microns of a *S. aureus*; this percentage decreases drastically to less than 40% for CSA-SNPs to *E. coli*. CSA-SNPs also show a higher incidence at distances greater than 5 microns for *E. coli* relative to *S. aureus*. This is confirmed by the averages and standard deviations in table 3.2; CSA-SNPs, on average, are closer to *S. aureus* than *E. coli*. The standard deviations indicate less dispersion amongst the CSA-SNP to *S. aureus* data than that to *E. coli*. A student's T-Test confirms that there is a statistically significant difference between the mean distances of CSA-SNPs to *S. aureus* and CSA-SNPs to *E. coli*. Ripley's K-function clustering analysis indicates that the CSA-SNPs are spatially clustered, particularly on shorter scales.

The negative control data shows no significant difference between the SNP to *S. aureus* distance and the SNP to *E. coli* distance. This is highlighted by large standard deviations for both negative control groups. However, the mean CSA-SNP to *S. aureus* distance is statistically significantly different than the SNP to *S. aureus* average distance.

Selectivity was then qualitatively demonstrated through video observation and optical trapping technology. Optical tweezers are capable of manipulating living cells and nanoparticles by placing pico Newton forces upon them by focusing a laser beam through a microscope objective. The beam waist, which is the narrowest part of the focused beam, contains a light gradient. The gradient attracts dielectric particles to the center of the beam. The highly focused infrared laser is positioned in this area and an optical trap is created. Optical trapping has the capability to manipulate small biological objects such as single bacterial cells as well as nanoparticles. The wavelength does not harm living cells. The optical trapping at cellular level provides insight into biological interactions. Optical

trapping of CSA-SNP and *staphylococcus aureus* were visualized in manipulated to show particular selectivity for one another.

Video clip 1 is a 300 frame-length movie. The compressed video clip can be replayed clip by clip in Window Media Player frame by frame. Initially *S. aureus* is trapped in the left upper corner and a CSA-NP is trapped in the middle of the screen. The interesting spot of reference is frames 139-158; the *S. aureus* is manipulated to slowly approach the CSA-NP and allowed to incubate for 1.2 seconds. The trap is then moved but staph is adhered to CSA-124. In frames 200-215 and 250-285 the same procedure is repeated and another two more bacteria adhere to the same CSA-NP.

An optical trap was used to show the adhesion of CSA-NP to *S. aureus*. A single bacterium was trapped in one specific trap and CSA-NP was trapped in another simultaneous trap. The bacteria were manually moved to approach the CSA-NP. The bacterium was then allowed to touch and incubate for a period less than two seconds. The two traps were then moved apart. The result was the *S. aureus* remained attached and was not able to be pulled apart by the force of the optical trap. The video shows that three separate bacteria can attach and bind two one CSA functionalized particle. The procedure was repeated with nanoparticles lacking CSA-124 surfactant. The nanoparticles without CSA-124 did not allow *S. aureus* to adhere.

3.4 Conclusion

Recent research indicates that there are potential downsides to indiscriminate use of broad spectrum antimicrobials. Off target effects can wipe out the body's natural microbial fauna, leaving niches available for opportunistic pathogen invasion, leading to

longer recovery times and the possibility of additional infection. Furthermore, by exposing the body's many bacterial strains to sub biocidal concentrations of broad spectrum antimicrobial, one increases the risk that these pressures will cause the development of new resistant strains. Increased affinity of an antimicrobial towards its target also potentially reduces the required effective dosage, increasing therapeutic index

Silver has been used clinically as a broad spectrum antimicrobial since it was approved by the FDA in the 1920s[88]. Resent research however, indicates that there are many downsides to indiscriminate antimicrobials including longer recovery times, increased risk of further infection, and higher incidence drug resistance. The data presented in this report suggests that the antimicrobial qualities of silver can be complemented, as well as made more selective toward specific classes of bacteria via conjugation with selective ligands such as CSA-124. Silver alone has MIC's of 120 ppm against both *S. aureus* and *E. coli* whereas CSA-SNPs express an MIC of 15 ppm and 30ppm toward *S. aureus* and *E. faecalis* respectively and an MIC of 30 ppm and 60ppm toward *E. coli* and *P. aeruginosa* respectively. These findings were further supported through MATLAB analysis of confocal images, indicating that while in co-culture 70% of CSA-SNPs were within 2 microns of *S. aureus* while less than 40% were within 2 microns of an *E. coli*. Video images of laser captured nanoparticle interactions with both bacteria also show clear selectivity for the gram positive *S. aureus* over the gram negative *E. coli*. Future work will focus on optimizing ligand concentration, verifying the mechanism of ligand affinity, and improving compatibility.

3.5 References

1. Mahmoudi, M., et al., *Toxicity Evaluations of Superparamagnetic Iron Oxide Nanoparticles: Cell "Vision" versus Physicochemical Properties of Nanoparticles.* Acs Nano, 2011. **5**(9): p. 7263-7276.

2. Kim, J.S., et al., *Antimicrobial effects of silver nanoparticles.* Nanomedicine-Nanotechnology Biology and Medicine, 2007. **3**(1): p. 95-101.

3. Agasti, S.S., et al., *Photoregulated Release of Caged Anticancer Drugs from Gold Nanoparticles.* Journal of the American Chemical Society, 2009. **131**(16): p. 5728-+.

4. Nakanishi, J., et al., *Light-Regulated Activation of Cellular Signaling by Gold Nanoparticles That Capture and Release Amines.* Journal of the American Chemical Society, 2009. **131**(11): p. 3822-+.

5. O'Neal, D.P., et al., *Photo-thermal tumor ablation in mice using near infrared-absorbing nanoparticles.* Cancer Letters, 2004. **209**(2): p. 171-176.

6. Cheng, K., et al., *Magnetic Targeting Enhances Engraftment and Functional Benefit of Iron-Labeled Cardiosphere-Derived Cells in Myocardial Infarction.* Circulation Research, 2010. **106**(10): p. 1570-U54.

7. Chertok, B., et al., *Iron oxide nanoparticles as a drug delivery vehicle for MRI monitored magnetic targeting of brain tumors.* Biomaterials, 2008. **29**(4): p. 487-496.

8. Yong, K.T., et al., *Synthesis and plasmonic properties of silver and gold nanoshells on polystyrene cores of different size and of gold-silver core-shell nanostructures.* Colloids and Surfaces a-Physicochemical and Engineering Aspects, 2006. **290**(1-3): p. 89-105.

9. Jackson, J.B. and N.J. Halas, *Silver nanoshells: Variations in morphologies and optical properties.* Journal of Physical Chemistry B, 2001. **105**(14): p. 2743-2746.

10. Pal, S., Y.K. Tak, and J.M. Song, *Does the antibacterial activity of silver nanoparticles depend on the shape of the nanoparticle? A study of the gram-negative bacterium Escherichia coli.* Applied and environmental microbiology, 2007. **73**(6): p. 1712-1720.

11. Chen, X., Gambhir, Sanjiv, *Theranostic Nanomedicine Editorial.* Accounts of Chemical Research 2011. **44**(10): p. 841-1134.

12. Narayanan, S.e.a., *Biocompatible Magnetite/Gold Nanohybrid Contrast Agents via Green Chemistry for MRI and CT Bioimaging.* Applied Material Interfaces, 2011. **ASAP**.

13. Yu, M.K., et al., *Drug-Loaded Superparamagnetic Iron Oxide Nanoparticles for Combined Cancer Imaging and Therapy In Vivo.* Angewandte Chemie International Edition, 2008. **47**(29): p. 5362-5365.

14. Yoo, D., et al., *Theranostic magnetic nanoparticles.* Accounts of chemical research, 2011. **44**(10): p. 863-874.

15. Jose L. Del Pozo, R.T., *Infection Associated with Prosthetic Joints.* The New England Jounral of Medicine, 2009(361): p. 787-794.

16. Hickok, N.J. and I.M. Shapiro, *Immobilized antibiotics to prevent orthopedic implant infections.* Advanced Drug Delivery Reviews, 2012.

17. Chiu, F.Y., et al., *Cefuroxime-Impregnated Cement in Primary Total Knee Arthroplasty A Prospective, Randomized Study of Three Hundred and Forty Knees.* The Journal of Bone & Joint Surgery, 2002. **84**(5): p. 759-762.

18. Emerich, D.F. and C.G. Thanos, *The pinpoint promise of nanoparticle-based drug delivery and molecular diagnosis.* Biomolecular Engineering, 2006. **23**(4): p. 171-184.

19. Chertok, B., et al., *Iron oxide nanoparticles as a drug delivery vehicle for MRI monitored magnetic targeting of brain tumors.* Biomaterials, 2008. **29**(4): p. 487-496.

20. Narayanan, S., et al., *Biocompatible magnetite/gold nanohybrid contrast agents via green chemistry for MRI and CT bioimaging.* ACS Applied Materials & Interfaces, 2011. **4**(1): p. 251-260.

21. Jung, W.K., et al., *Antibacterial activity and mechanism of action of the silver ion in Staphylococcus aureus and Escherichia coli.* Applied and Environmental Microbiology, 2008. **74**(7): p. 2171-2178.

22. Bosetti, M., et al., *Silver coated materials for external fixation devices: in vitro biocompatibility and genotoxicity.* Biomaterials, 2002. **23**(3): p. 887-892.

23. Qureshi, A.T., et al., *Biocompatible/bioabsorbable silver nanocomposite coatings.* Journal of Applied Polymer Science, 2011. **120**(5): p. 3042-3053.

24. Popovtzer, R., et al., *Targeted gold nanoparticles enable molecular CT imaging of cancer.* Nano letters, 2008. **8**(12): p. 4593-4596.

25. Babes, L., et al., *Synthesis of iron oxide nanoparticles used as MRI contrast agents: A parametric study.* Journal of Colloid and Interface Science, 1999. **212**(2): p. 474-482.

26. Alves, K.G., et al., *Magnetite/Polypyrrole Hybrid Nanocomposites as a Promising Magnetic Resonance Imaging Contrast Material.* Journal of Applied Polymer Science, 2012.

27. Na, H.B., I.C. Song, and T. Hyeon, *Inorganic Nanoparticles for MRI Contrast Agents.* Advanced Materials, 2009. **21**(21): p. 2133-2148.

28. Bonnemain, B., *Superparamagnetic Agents in magnetic resonance imaging: physicochemical characteristics and clinical applications a review.* Journal of drug targeting, 1998. **6**(3): p. 167-174.

29. Schweiger, C., et al., *MRI contrast enhancement potential of different superparamagnetic iron oxide nanoparticle (SPION) formulations.* Journal of Controlled Release, 2010. **148**(1): p. E67-E68.

30. Moghadam, B.Y., et al., *The Role of Nanoparticle Surface Functionality in the Disruption of Model Cell Membranes.* Langmuir, 2012.

31. Perry, J., et al., *PEGylated PRINT Nanoparticles: The Impact of PEG Density on Protein Binding, Macrophage Association, Biodistribution, and Pharmacokinetics.* Nano Letters, 2012.

32. Garza-Ocañas, L., et al., *Biodistribution and long-term fate of silver nanoparticles functionalized with bovine serum albumin in rats.* Metallomics, 2010. **2**(3): p. 204-210.

33. Sadauskas, E., et al., *Kupffer cells are central in the removal of nanoparticles from the organism.* Part Fibre Toxicol, 2007. **4**(10): p. 10.

34. Takenaka, E.K., W. Möller, C. Roth, A. Ziesenis, U. Heinzmann, P. Schramel, J. Heyder, S, *A morphologic study on the fate of ultrafine silver particles: Distribution pattern of phagocytized metallic silver in vitro and in vivo.* Inhalation Toxicology, 2000. **12**(S3): p. 291-299.

35. Ling, M.M., K.Y. Wang, and T.S. Chung, *Highly Water-Soluble Magnetic Nanoparticles as Novel Draw Solutes in Forward Osmosis for Water Reuse.* Industrial & Engineering Chemistry Research, 2010. **49**(12): p. 5869-5876.

36. Abdel-Halim, E. and S.S. Al-Deyab, *Utilization of hydroxypropyl cellulose for green and efficient synthesis of silver nanoparticles.* Carbohydrate polymers, 2011. **86**(4): p. 1615-1622.

37. Bilbao-Sáinz, C., et al., *Composite edible films based on hydroxypropyl methylcellulose reinforced with microcrystalline cellulose nanoparticles.* Journal of agricultural and food chemistry, 2010. **58**(6): p. 3753-3760.

38. Mergel, M., *Polyacrylic Acid*, S.G. Gilbert, Editor 2010, Toxipedia.

39. Nancy M. Franson, D.R.S., *Milled naproxen with hydroxypropyl cellulose as a dispersion stabilizer*, USPTO, Editor 1997, NanoSystems L.L.C., Collegeville, PA: USA.

40. Ain-Ai, A. and P.K. Gupta, *Effect of arginine hydrochloride and hydroxypropyl cellulose as stabilizers on the physical stability of high drug loading nanosuspensions of a poorly soluble compound.* International journal of pharmaceutics, 2008. **351**(1): p. 282-288.

41. Williams, R., *HYDROXYPROPYL CELLULOSE*, in *Material Safety Data Sheet:*2001, USP.

42. SIGMA-ALDRICH, *POLY(ACRYLIC ACID)*, in *MATERIAL SAFETY DATA SHEET*2006: 3050 Spruce Street SAINT LOUIS MO 63103 US.

43. Leszczynska, K., et al., *Bactericidal activities of the cationic steroid CSA-13 and the cathelicidin peptide LL-37 against Helicobacter pylori in simulated gastric juice.* Bmc Microbiology, 2009. **9**.

44. Bucki, R., et al., *Resistance of the antibacterial agent ceragenin CSA-13 to inactivation by DNA or F-actin and its activity in cystic fibrosis sputum.* Journal of Antimicrobial Chemotherapy, 2007. **60**(3): p. 535-545.

45. Leszczynska, K., et al., *Potential of ceragenin CSA-13 and its mixture with pluronic F-127 as treatment of topical bacterial infections.* Journal of Applied Microbiology, 2011. **110**(1): p. 229-238.

46. Becker, R.O., *Silver ions in the treatment of local infections.* Metal-based drugs, 1999. **6**(4-5): p. 311.

47. Katz, E. and I. Willner, *Integrated nanoparticle-biomolecule hybrid systems: Synthesis, properties, and applications.* Angewandte Chemie-International Edition, 2004. **43**(45): p. 6042-6108.

48. Ghosh, P., et al., *Gold nanoparticles in delivery applications.* Advanced Drug Delivery Reviews, 2008. **60**(11): p. 1307-1315.

49. Seferos, D.S., et al., *Polyvalent DNA Nanoparticle Conjugates Stabilize Nucleic Acids.* Nano Letters, 2009. **9**(1): p. 308-311.

50. Brust, M., et al., *Synthesis of thiol-derivatised gold nanoparticles in a two-phase Liquid–Liquid system.* Journal of the Chemical Society, Chemical Communications, 1994. **1994**(7): p. 801-802.

51. Lattuada, M. and T.A. Hatton, *Functionalization of monodisperse magnetic nanoparticles.* Langmuir, 2007. **23**(4): p. 2158-2168.

52. Grabarek, Z. and J. Gergely, *ZERO-LENGTH CROSSLINKING PROCEDURE WITH THE USE OF ACTIVE ESTERS.* Analytical Biochemistry, 1990. **185**(1): p. 131-135.

53. Tengvall, P., et al., *Preparation of multilayer plasma protein films on silicon by EDC/NHS coupling chemistry.* Colloids and Surfaces B-Biointerfaces, 2003. **28**(4): p. 261-272.

54. Merlic, C. *IR Absorption Table*. WebSpectra 2000 [cited 2011 5 Dec 2011]; Available from: http://www.chem.ucla.edu/~webspectra/irtable.html.

55. Dutz, S., et al., *Hysteresis losses of magnetic nanoparticle powders in the single domain size range.* Journal of Magnetism and Magnetic Materials, 2007. **308**(2): p. 305-312.

56. Vuong, Q.L., et al., *A Universal Scaling Law to Predict the Efficiency of Magnetic Nanoparticles as MRI T2-Contrast Agents.* Advanced healthcare materials, 2012. **1**(4): p. 502-512.

57. Guarner, F. and J.-R. Malagelada, *Gut flora in health and disease.* Lancet (London, England), 2003. **361**(9356): p. 512-519.

58. Kelly, C.P., C. Pothoulakis, and J.T. LaMont, *Clostridium difficile colitis.* New England Journal of Medicine, 1994. **330**(4): p. 257-262.

59. Bignardi, G., *Risk factors for Clostridium difficile infection.* The Journal of hospital infection, 1998. **40**(1): p. 1.

60. Eckert, R., et al., *Targeted killing of Streptococcus mutans by a pheromone-guided "smart" antimicrobial peptide.* Antimicrobial Agents and Chemotherapy, 2006. **50**(11): p. 3651-3657.

61. Travan, A., et al., *Non-cytotoxic silver nanoparticle-polysaccharide nanocomposites with antimicrobial activity.* Biomacromolecules, 2009. **10**(6): p. 1429-1435.

62. Yih, T. and M. Al-Fandi, *Engineered nanoparticles as precise drug delivery systems.* Journal of cellular biochemistry, 2006. **97**(6): p. 1184-1190.

63. Minchin, R.F. and D.J. Martin, *Minireview: nanoparticles for molecular imaging—an overview.* Endocrinology, 2010. **151**(2): p. 474-481.

64. Singh, R. and J.W. Lillard Jr, *Nanoparticle-based targeted drug delivery.* Experimental and molecular pathology, 2009. **86**(3): p. 215-223.

65. Gelperina, S., et al., *The potential advantages of nanoparticle drug delivery systems in chemotherapy of tuberculosis.* American journal of respiratory and critical care medicine, 2005. **172**(12): p. 1487-1490.

66. Love, J.C., et al., *Self-assembled monolayers of thiolates on metals as a form of nanotechnology.* Chemical Reviews-Columbus, 2005. **105**(4): p. 1103-1170.

67. Brown, P.K., et al., *Silver Nanoscale Antisense Drug Delivery System for Photoactivated Gene Silencing.* Acs Nano, 2013.

68. Kim, J.S., et al., *Antimicrobial effects of silver nanoparticles.* Nanomedicine: Nanotechnology, Biology and Medicine, 2007. **3**(1): p. 95-101.

69. Lok, C.-N., et al., *Silver nanoparticles: partial oxidation and antibacterial activities.* Journal of Biological Inorganic Chemistry, 2007. **12**(4): p. 527-534.

70. Rai, M., A. Yadav, and A. Gade, *Silver nanoparticles as a new generation of antimicrobials.* Biotechnology advances, 2009. **27**(1): p. 76-83.

71. Aymonier, C., et al., *Hybrids of silver nanoparticles with amphiphilic hyperbranched macromolecules exhibiting antimicrobial properties.* Chemical Communications, 2002(24): p. 3018-3019.

72. Gibbins, B. and L. Warner, *The role of antimicrobial silver nanotechnology.* Medical Device & Diagnostic Industry Magazine, 2005. **1**: p. 1-2.

73. Silver, S., L.T. Phung, and G. Silver, *Silver as biocides in burn and wound dressings and bacterial resistance to silver compounds.* Journal of industrial microbiology & biotechnology, 2006. **33**(7): p. 627-634.

74. Hancock, R. and A. Patrzykat, *Clinical development of cationic antimicrobial peptides: from natural to novel antibiotics.* Current drug targets-Infectious disorders, 2002. **2**(1): p. 79-83.

75. Zasloff, M., *Antimicrobial peptides of multicellular organisms.* Nature, 2002. **415**(6870): p. 389-395.

76. Epand, R.M., R.F. Epand, and P.B. Savage, *Ceragenins (cationic steroid compounds), a novel class of antimicrobial agents.* Drug News Perspect, 2008. **21**(6): p. 307-11.

77. Chin, J.N., et al., *Potential synergy activity of the novel ceragenin, CSA-13, against clinical isolates of Pseudomonas aeruginosa, including multidrug-resistant P. aeruginosa.* Journal of antimicrobial chemotherapy, 2008. **61**(2): p. 365-370.

78. Leszczyńska, K., et al., *Bactericidal activities of the cationic steroid CSA-13 and the cathelicidin peptide LL-37 against Helicobacter pylori in simulated gastric juice.* BMC microbiology, 2009. **9**(1): p. 187.

79. Chin, J.N., et al., *Antimicrobial activities of ceragenins against clinical isolates of resistant Staphylococcus aureus.* Antimicrobial agents and chemotherapy, 2007. **51**(4): p. 1268-1273.

80. Leszczyńska, K., et al., *Antibacterial activity of the human host defence peptide LL-37 and selected synthetic cationic lipids against bacteria associated with oral and upper respiratory tract infections.* Journal of Antimicrobial Chemotherapy, 2013. **68**(3): p. 610-618.

81. Andrews, J.M., *Determination of minimum inhibitory concentrations.* Journal of Antimicrobial Chemotherapy, 2001. **48**(suppl 1): p. 5-16.

82. Wiegand, I., K. Hilpert, and R.E. Hancock, *Agar and broth dilution methods to determine the minimal inhibitory concentration (MIC) of antimicrobial substances.* Nature protocols, 2008. **3**(2): p. 163-175.

83. WallertandProvostLab. *Proliferation Assay: MTT Protocol*. 2007; Available from: http://www.mnstate.edu/provost/MTT_Proliferation_Protocol.pdf.

84. de Nooijer, L.J., I. Duijnstee, and G. Van der Zwaan, *Novel application of MTT reduction: a viability assay for temperate shallow-water benthic foraminifera.* The Journal of Foraminiferal Research, 2006. **36**(3): p. 195-200.

85. Taylor, P., et al., *Determination of minimum bactericidal concentrations of oxacillin for Staphylococcus aureus: influence and significance of technical factors.* Antimicrobial Agents and Chemotherapy, 1983. **23**(1): p. 142-150.

86. Morones, J.R., et al., *The bactericidal effect of silver nanoparticles.* Nanotechnology, 2005. **16**(10): p. 2346.

87. Ruparelia, J.P., et al., *Strain specificity in antimicrobial activity of silver and copper nanoparticles.* Acta Biomaterialia, 2008. **4**(3): p. 707-716.

88. Jain, J., et al., *Silver nanoparticles in therapeutics: development of an antimicrobial gel formulation for topical use.* Molecular Pharmaceutics, 2009. **6**(5): p. 1388-1401.

CHAPTER 4. CONCLUSIONS AND FUTURE WORK

4.1 Conclusion

Chapter 2 demonstrated a proof of concept for diagnostic, antimicrobial nanoparticles comprised of a maghemite core, gold nano-seeds, silver shell, and CSA-124 surface molecules. Characterization through numerous methods advocates that the synthesis process described successfully generates the proposed product. The FT-IR spectrums support the addition of a mercapto group to the Fe-PAA NP. ICP-OES demonstrated the final product is comprised of 76.64% silver, 22.75% iron, and 0.61% gold with ~8% total yield. Both TEM and DLS results demonstrate predictable growth of the particle with each additive process step. These results, along with the UV-vis spectra indicate that gold and silver were successfully deposited onto the Fe-PAA NPs, yielding a final nanoparticle of 32.474 $^{+}$/- 1.83 nm diameter and 53.053 $^{+}$/- 1.202 nm hydrodynamic diameter. Furthermore, these particles were shown to be predominantly paramagnetic and possess a strong magnetic moment of 54 emu/g Fe due to their maghemite core; characteristics representative of clinically used T2 MRI contrast agents, making DANs a good candidate for diagnostic use. MRI of DANs and maghemite core NPs at various concentrations suggest a 16.7 gray scale unit reduction in pixel intensity for each ppm DAN and significant contrast with as little as 9 ppm. DANs have also demonstrated an ability to adhere and contrast *S. aureus in vitro*. The results presented in the report indicate DANs to be a potentially viable diagnostic contrast agent for deep tissue infection

The data presented in chapter 3 suggests that the antimicrobial qualities of silver can be complemented as well as focused toward specific classes of bacteria via conjugation with selective ligands such as CSA-124. Silver alone has MIC's of 120 ppm against both *S. aureus* and *E. coli* whereas CSA-SNPs express an MIC of 15 ppm and 30ppm toward *S. aureus and E. faecalis* respectively and an MIC of 30 ppm and 60ppm toward *E. coli* and *P. aeruginosa* respectively. These findings were further supported through MATLAB analysis of confocal images, indicating that while in co-culture 70% of CSA-SNPs were within 2 microns *of S. aureus* while less than 40% were within 2 microns of an *E. coli*. Video of laser captured nanoparticle interactions with both bacteria also show clear selectivity for the gram positive *S. aureus* over the gram negative *E. coli*. CSA-SNPs have however shown to be relatively cytotoxic and hemolytic with a therapeutic index of roughly 3.

4.2 Future Work

While this report has demonstrated a very promising proof of concept, there is much optimization to be done with regard to both DANs and CSA-SNPs. Synthesis of the DAN core should be adjusted to yield only particles under 10 nm or a separation step will need to be added to remove larger, ferromagnetic particles, thus making DANs 100% paramagnetic. Additionally, there are many other paramagnetic contrast compounds that could be employed as the DAN core to make a T1 contrasting DAN. Future work should include additional in vitro MRI testing using a more complex tissue phantom.

The other major parameter in need of optimization is that of the surface molecule attachment. The proper number of CSA-124s to be attached for optimal antimicrobial,

selective, and cytotoxic characteristics should be assessed. Also, exploring other selective surface molecules may be necessary if CSA-124 proves to be too toxic or not adequately selective. Work can be done in encapsulating CSA-124s in liposomes. This would decrease cytotoxicity as well as provide longer circulation time *in vivo.* Lastly, once the necessary optimizations have been achieved and the cytotoxic and hemolytic qualities have been minimized, an animal trial could be conducted to access the full potential of the conjugate nanoparticles.

VITA

Mark Hoppens grew up in Slidell, Louisiana. He attended Louisiana State University in Baton Rouge for seven years, earning a Bachelor's of Science in Biological & Agricultural Engineering in 2011 and a Master's of Science in Biological & Agricultural Engineering in 2013. He plans to attend medical school in the fall of 2014.